Urca cooling of the neutron star in the Cassiopeia A supernova remnant

A.Y. Potekhin[a,*], D.G. Yakovlev[a]

[a]*Ioffe Institute, Politekhnicheskaya 26, Saint Petersburg, 194021, Russia*

Abstract

Observed cooling rate of the young neutron star (NS) in the Cassiopeia A supernova remnant (Cas A NS) exceeds theoretical expectations based on conventional scenarios of NS cooling, controlled mainly by modified Urca (mUrca) neutrino emission. Several hypotheses have been suggested to explain these observations. The most popular one assumes the cooling enhancement by neutrino emission due to the Cooper pair breaking and formation (PBF) just after the onset of neutron superfluidity in the NS core. This explanation requires strict constraints on critical temperatures of proton and neutron superfluidities in the NS core and on the efficiency of the PBF cooling mechanism. These constraints are in tension with the modern theory. To relax them, Lev Leinson (2022) suggested a hybrid cooling scenario, where the direct Urca (dUrca) process of neutrino emission from a small NS central kernel contributes to the cooling enhancement in addition to the PBF process. We show that Cas A NS cooling needs not to be hybrid, as the joint effect of Urca (dUrca+mUrca) processes can explain the observations equally well with or without superfluidity and the PBF mechanism. We explore the Urca scenario with different assumptions about NS equation of state, baryon superfluidity, and composition of the outer heat-blanketing envelope. We show that the observed cooling rate can be reproduced with many combinations of these assumptions by tuning the NS mass, which should slightly exceed the threshold mass for opening the dUrca process in the kernel. Then the core stays non-isothermal for centuries, delaying the onset of enhanced dUrca cooling to satisfy the Cas A NS observations. In addition, we present an analytic toy model which elucidates many features of the Urca scenario.

Keywords: stars: neutron, dense matter, neutrinos, X-rays: stars, stars: individual: CXOU J232327.8+584842

1. Introduction

Thermal radiation of neutron stars (NSs) provides insight into their superdense interiors. NS cooling depends on NS mass, equation of state (EoS), composition and microphysics of its core and outer layers. Therefore a comparison of NS cooling theory with observations can help one to determine some parameters of NSs and to choose among theoretical models of superdense matter. A particularly challenging object for such studies is the central compact object in the Cassiopeia A supernova remnant (SNR Cas A, G111.7−02.1) – CXOU J232327.8+584842, aka Cas A NS. It is the youngest known NS in our Galaxy. Ashworth (1980) attributed the SNR Cas A to the supernova observed by Flamsteed on August 16, 1680; this attribution was corroborated by an independent evaluation of the SNR age by Fesen et al. (2006). The distance to the SNR Cas A is $d = 3.4^{+0.3}_{-0.1}$ kpc (Reed et al., 1995).

The Cas A NS belongs to a small class of X-ray thermal isolated NSs (XTINSs), which show neither radio nor gamma-ray emission, nor other signs of magnetospheric activity, but emit purely thermal soft X-ray radiation. A tight upper limit on its pulsations (Pavlov and Luna, 2009) disfavors substantial large-scale temperature variations over its surface.

The Cas A NS was the first NS whose spectrum was successfully fitted by the carbon atmosphere model (Ho and Heinke, 2009). Since then, several other NS spectra have been fitted by carbon atmosphere models (see Alford and Halpern 2023 for references and discussion). The Cas A NS is most intriguing among these objects because of a measured decrease of its effective surface temperature T_s, derived from observations by the *Chandra* X-ray observatory since 2000. This apparent real-time cooling, first noticed by Heinke and Ho (2010), turns out to be more rapid than that predicted by conventional cooling models for NSs of its age. Page et al. (2011) and Shternin et al. (2011) suggested that this cooling enhancement could be due to Cooper pair breaking and formation (PBF) in the triplet channel of neutron superfluidity, which had appeared in the NS core. Other hypothetical explanations include: thermal recovery after an episode of stellar oscillations (Yang et al., 2011), sudden onset of rapid direct Urca (dUrca) cooling caused by particle repopulation due to NS spin-down (Negreiros et al., 2013), suppression of thermal conductivities by medium effects in the NS core (Blaschke et al., 2012, 2013; Taranto et al., 2016), magnetic field decay (Bonanno et al., 2014), diffusive nuclear burning in a heat-blanketing envelope (Wijngaarden et al., 2019), cooling enhancement due to emission of axions (Leinson, 2014, 2021; Sedrakian, 2016a, 2019; Hamaguchi et al., 2018), phase transitions in a hypothetical quark core of a massive NS (Noda et al., 2013; Sedrakian, 2013, 2016b), or a cooling after a fall-back accretion with roto-chemical heating of the star containing quark matter (Wei et al., 2020). In some papers, hybrid scenarios have been proposed, such as the PBF mechanism supplemented either by emission of axions (Leinson, 2021) or

*Corresponding author.

Email addresses: palex-spb@yandex.ru (A.Y. Potekhin), yak@astro.ioffe.ru (D.G. Yakovlev)

by dUrca emission of neutrinos (Leinson, 2022, as discussed below).

The PBF neutrino emission in NSs was first considered by Flowers et al. (1976) and by Voskresensky and Senatorov (1987). If internal NS temperature T is below a critical temperature for superfluidity onset, $T_{\rm crit}$, the baryon fluid has two components: a superfluid condensate and quasiparticle excitations – broken Cooper pairs. Their quasi-equilibrium amount is mainly maintained by thermal spin and density fluctuations. However, recombination of broken pairs can also occur through an additional, much slower channel. It is mediated by weak neutral currents and results in the emission of neutrino pairs. The neutrino escape violates the energy balance between the endothermic pair breaking and exothermic pair formation events and cools the star. The PBF cooling is most powerful at T slightly below $T_{\rm crit}$. Practical formulae for the PBF neutrino emissivities have been presented by Yakovlev et al. (2001).

Leinson and Pérez (2006) noticed that the vector-current channel in the above-cited works lacks a critical suppression factor of $(v_{\rm F}/c)^4$, where $v_{\rm F}$ is the Fermi velocity and c is the speed of light. This suppression renders the singlet-pairing PBF contribution negligible in practice. The theory of vector-current neutrino emission from S-wave superfluid condensates has been further significantly advanced by Sedrakian et al. (2007); Kolomeitsev, Voskresensky (2008, 2010); Steiner and Reddy (2009); Leinson (2009); Sedrakian (2012).

The PBF mechanism remains viable for triplet pairing, which occurs through both vector and axial channels. A complete suppression of the vector channel with unchanged axial-vector channel implies that the neutrino emissivity due to triplet pairing of neutrons, given by Yakovlev et al. (2001), has to be multiplied by a factor $q_{\rm PBF} \approx 0.76$ (Leinson and Pérez, 2006).

Leinson (2010) has reanalysed the axial-vector channel of triplet pairing of neutrons by a consistent resummation of the leading-order diagrams, some of which had been missed in the earlier studies. This resummation ensures the conservation of vector current. As a result, the axial channel is suppressed by a factor of 1/4, so that $q_{\rm PBF} \approx 0.19$ instead of 0.76.

The PBF channel was first included in NS cooling simulations by Schaab et al. (1997). The cooling of the Cas A NS enhanced by this mechanism (Page et al., 2011; Shternin et al., 2011) has been widely used to constrain properties of nucleon superfluidity in the Cas A NS core (e.g., Ho et al., 2015; Taranto et al., 2016; Shternin et al., 2021, 2023). This explanation is appealing because it does not require any exotic assumptions about evolutionary path or core composition of the star. It can be successful if (1) neutron superfluidity develops in the core at such a temperature $T_{\rm core}$ which can be reconciled with observed surface temperatures $T_{\rm s}(t)$, (2) proton superfluidity is sufficiently strong to suppress modified Urca (mUrca) processes early enough for delaying the cooling to the required $T_{\rm core}$ at the present NS age (> 300 yr), and (3) the PBF mechanism is sufficiently strong to ensure the observed real-time cooling (Shternin et al., 2011, 2021, 2023; Ho et al., 2015). However, the second and third conditions are in tension with modern theory.

The second condition is problematic, because the most advanced theoretical results suggest that protons are nonsuperfluid in a large part of the NS core, as will be shown in Section 3.2. The third condition is in conflict with the above-mentioned reduction of the PBF reaction rate to a factor of $q_{\rm PBF} \approx 0.19$.

Page et al. (2011) and Ho et al. (2015) studied the PBF cooling scenario adopting the factor $q_{\rm PBF} = 0.76$ from Leinson and Pérez (2006), whereas Shternin et al. (2011, 2021, 2023) treated $q_{\rm PBF}$ as a free parameter. The latter authors found that the theory requires $q_{\rm PBF} > 0.4$–0.5 to be reconciled with the Cas A NS data, which is incompatible with $q_{\rm PBF} = 0.19$ derived by Leinson (2010).

To resolve this tension, Leinson (2022) suggested a hybrid cooling scenario, where PBF cooling was supplemented by dUrca cooling in a small central kernel of the NS core (hereinafter, *the dUrca kernel*). Recently, the same scenario has been studied by Tu and Li (2025), although they have added free hyperons to make dUrca processes possible in their EoS model. Other recent scenarios of the Cas A cooling involving a dUrca kernel include NSs described by a specific class of EoSs (EoS with induced surface tension, Tsiopelas and Sagun 2020, 2021) and NSs with admixture of dark matter (Avila et al., 2024).

According to the hybrid scenario of Cas A NS cooling, the dUrca kernel becomes cold very soon after the NS birth and it stays colder than the surrounding outer core for centuries. The enhanced dUrca cooling is inefficient for the global cooling till the temperature of the outer core equilibrates with the kernel temperature. This delay helps explaining the observed cooling rate, but only partly: an additional enhancement is required (e.g. superfluidity and PBF process). All these results have been obtained in numerical simulations, without explaining the prolonged existence of a cold kernel.

A comprehensive numerical study of such kernels have been conducted by Sales et al. (2020), who properly interpreted the phenomenon by the appearance of quasi-stationary thermal states in which the heat is thermally conducted into the kernel from the outside core and then radiated away by dUrca neutrinos, at slow rates because the kernel stays cold. To the best of our knowledge, the results of that publication have not been applied to the Cas A NS.

We propose that the presence of the dUrca kernel can reconcile theory with observations of the Cas A NS without any constraints on nucleon superfluidity or PBF processes and without involving exotic particles, special EoS models etc., although such effects can be easily incorporated. Nevertheless, the Urca scenario requires an adjustment of the size of the dUrca kernel, which can be achieved by NS mass tuning. However, every Cas A NS cooling scenario requires serious tuning of some NS model parameters anyway,

We also present an approximate analytical description of the considered Urca cooling scenario, which elucidates the role of heat flows in a non-isothermal NS core and reveals dependence of enhanced cooling on NS parameters.

The paper is organized as follows. In Section 2 we overview current status of the Cas A NS observations and compare their possible interpretations in terms of surface temperature or photon luminosity. In Section 3 we outline basic properties of superfluidity in NSs. In Section 4 we present numerical simula-

tions of Cas A NS cooling in frames of the PBF, hybrid, and Urca scenarios, confront them with observations and discuss corresponding constraints on microphysical theories of NS matter. In Section 5 and Appendix A we construct a toy model which allows one to estimate many parameters of Urca cooling (revealed numerically by Sales et al. 2020). Conclusions are formulated in Section 6.

2. Cas A NS cooling inferred from observations

Cooling of the Cas A NS has been the topic of continued interest and X-ray monitoring after Heinke and Ho (2010) reported an unexpectedly rapid decline of its effective surface temperature T_s. Those results were based on spectral fits using a model of a non-magnetic carbon atmosphere, which covered the whole NS surface with a uniform effective temperature. The data were obtained from observations with the Advanced CCD Imaging Spectrometer (ACIS) onboard *Chandra* observatory. Later they have been supplemented and improved on the base of continued observations and refined calibration (Elshamouty et al., 2013; Posselt et al., 2013; Ho et al., 2015, 2021; Posselt and Pavlov, 2018, 2022; Wijngaarden et al., 2019; Shternin et al., 2023). In particular, Posselt et al. (2013) and Posselt and Pavlov (2018, 2022) pointed out that observations were mostly performed in the ACIS-S Graded telemetry mode, aimed primarily at studying the SNR, and argued that this mode suffered from several instrumental effects. They suggested that the Faint subarray mode would be preferable, because it minimizes some spectrum-distorting effects such as pileup. The authors found a significant difference in absolute values and a marginally different decline of the effective temperature, obtained using the two modes separately. To take the former difference into account, Shternin et al. (2023) introduced a calibration factor $A \approx 1.08$ into a spectral model for the Graded mode data, which allowed them to perform a joint analysis of all ACIS observations.

Fig. 1a shows some recent results of the analysis of Cas A NS observations (Wijngaarden et al., 2019; Posselt and Pavlov, 2022; Shternin et al., 2023). Specifically, Wijngaarden et al. (2019) analyzed the *Chandra* ACIS-S Graded mode observations from 2000 to 2018. They estimated the NS mass $M = 1.65 \pm 0.16\,M_\odot$ and radius $R = 12.94 \pm 0.34$ km. Then they analyzed variation of T_s with M and R fixed to the best-fit values using the hydrogen column density N_H either assumed to be constant for all observations or freely varied between them. Also, they performed an analysis without allowing N_H to vary between observations and with the best-fit values $M = 1.65\,M_\odot$ and $R = 10.3$ from the previous analysis (Elshamouty et al., 2013). Ho et al. (2021) reanalyzed the data including a more recent *Chandra* observation (2019) in the Graded mode and using improvements in ACIS calibration. The results appeared consistent with the previous ones. Posselt and Pavlov (2022) included the observations of 2020 in the Faint mode and reanalyzed the observations in the Faint and Graded modes separately, with N_H either freely varied or fixed across observations. They confirmed their previous finding (Posselt and Pavlov, 2018) that ACIS Faint mode data suggested a systematically higher T_s and somewhat smaller decrease of T_s than those obtained in Graded mode. Shternin et al. (2023) performed a joint analysis of all ACIS observations in the Graded and Faint modes. They showed that the results of the spectral analysis of the Faint mode data were consistent with those for the Graded mode (up to the calibration factor $A = 1.08$ mentioned above).

The estimates of T_s in Fig. 1a exhibit systematic differences within $\sim 20\%$ between different NS models employed. Within each model, one sees a significant gradual decrease of T_s with time. It can be described by

$$\log T_s(t) = \log T_s(t_0) - s \log(t/t_0), \quad (1)$$

where $t_0 = 330$ yr is chosen as the representative Cas A NS age t in the current epoch, and the slope s is a fit parameter. Open and filled circles in the figure represent the data of Tables 1 and 2 of Shternin et al. (2023) for spectral fitting with fixed NS parameters (specified in the caption of Fig. 1), with constant or varying N_H, respectively. In addition to this 'simplified' analysis, Shternin et al. (2023) have performed a complex Bayesian analysis of Faint and Graded mode observations, jointly and separately, assuming either constant or varying N_H. The wide vertical black errorbar in Fig. 1a embraces their estimates of $T_s(t_0)$ at 68% credibility level (that will also be called 1σ interval, for brevity) for both hypotheses on N_H variability, but only for the joint analysis of all the data. The results of separate analyses have a much larger scatter. Shternin et al. (2023) have concluded that the surface temperature decline is $2.12 \pm 0.3\%$ or $1.6 \pm 0.2\%$ in 10 yr for variable or fixed N_H model, respectively. The authors have estimated the Cas A NS mass and radius as $M = 1.55 \pm 0.25\,M_\odot$ and $R = 13.5 \pm 1.5$ km. The shaded region in Fig. 1a shows the range of $T_s(t)$ according to Eq. (1) with the slope s varying within any of these estimates (i.e., from 0.466 to 0.801) while keeping $T_s(t_0)$ fixed at the center of the errorbar.

For NSs with well determined distance, the photon luminosity L_γ can be a better choice than the surface temperature T_s for comparing with cooling theory (see Potekhin et al. 2020, for a discussion). Fig. 1b confirms this statement for the Cas A NS. Here, the data points with errorbars show bolometric photon luminosities calculated using the data presented in Fig. 1a,

$$L_\gamma = 4\pi\sigma_{SB} T_s^4 R^2, \quad (2)$$

where σ_{SB} is the Stefan-Boltzmann constant. We see that different data sets differ by less than 30%, despite strong T_s-dependence in Eq. (2). According to this dependence, the shaded area covers a slope range $s_L = 4s$. The black errorbar at $t = t_0$ embraces estimates of $L_\gamma(t_0)$ at the 68% credibility level for both hypotheses on the N_H variability. They are derived according to Eq. (2) from the estimates of $T_s(t_0)$ and R and their uncertainties, taking into account T_s–R anticorrelation (Shternin et al., 2023). This anticorrelation reduces the joint 1σ luminosity interval to $L_\gamma(t_0) \in [1.06 \times 10^{34}, 1.22 \times 10^{34}]$ erg s^{-1}.

The quantities T_s and L_γ in Eq. (2) refer to a local reference frame at the NS surface. The quantities detected by a distant observer are redshifted (e.g., Thorne 1977), as labeled by tilde

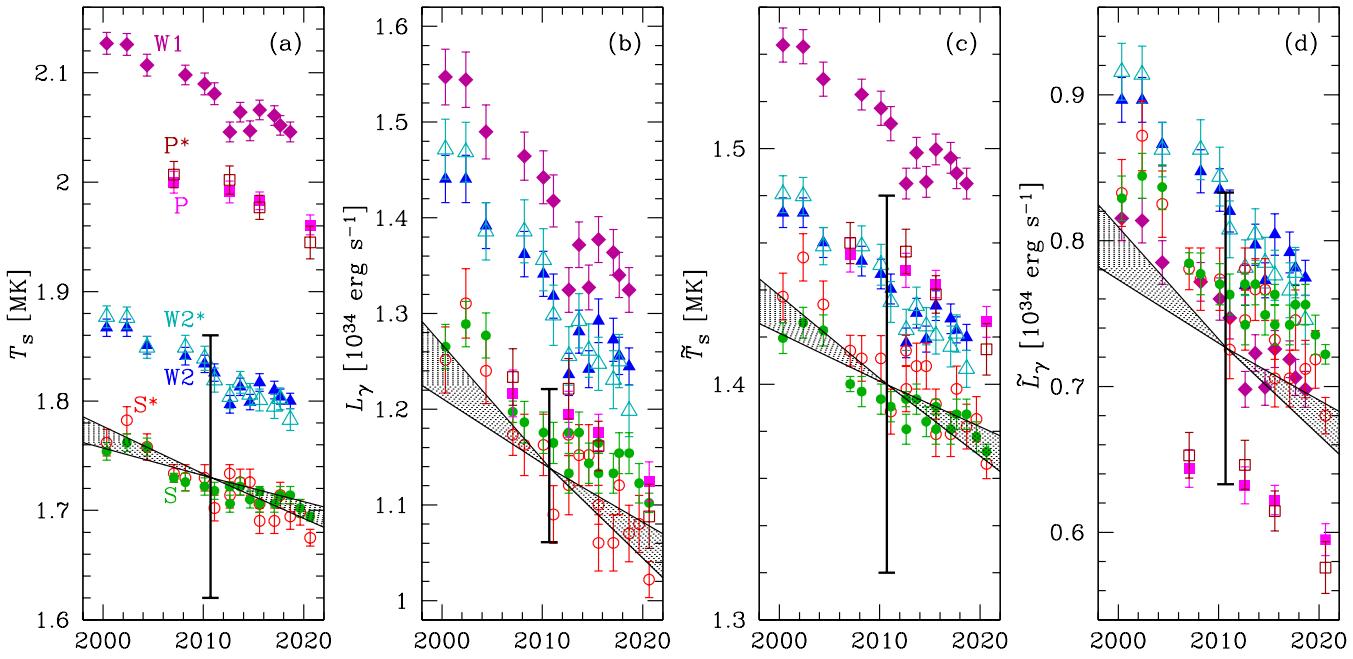

Figure 1: Estimates of Cas A NS thermal radiation versus observation year, according to *Chandra* observations analyzed using carbon NS atmosphere models by three groups, labeled W, P, and S. Group W: Wijngaarden et al. (2019), ACIS-S Graded mode observations from 2000 to 2018. Group P: Posselt and Pavlov (2022), Faint mode observations from 2006 to 2020. Group S: Shternin et al. (2023), all observations (2000–2020). Symbols with errorbars mark employed theoretical models. **Panel (a):** Effective surface temperature in 10^6 K. W1, filled diamonds: $M = 1.65\,M_\odot$, $R = 10.3$ km, fixed $N_{\rm H}$. W2, filled triangles: $M = 1.65\,M_\odot$, $R = 12.9$ km, fixed $N_{\rm H}$. W2, empty triangles: $M = 1.65\,M_\odot$, $R = 12.9$ km, variable $N_{\rm H}$. In these three cases the distance d is fixed at 3.4 kpc. P, filled squares: $M = 1.647\,M_\odot$, $R = 10.33$ km, $d = 3.4$ kpc, fixed $N_{\rm H}$. P*, empty squares: same as P but variable $N_{\rm H}$. S, heavy dark-green dots: $M = 1.60\,M_\odot$, $R = 13.7$ km, $d = 3.33$ kpc, fixed $N_{\rm H}$. S^*, empty red circles: $M = 1.53\,M_\odot$, $R = 13.5$ km, $d = 3.33$ kpc, variable $N_{\rm H}$. The shaded area illustrates the regression model (1) with the range s of $T_{\rm s}$ decline that embraces 68% credible intervals obtained by the joint ACIS data analysis (Shternin et al., 2023). Wide black vertical errorbar embraces 68% uncertainties for $T_{\rm s}$ at the age $t_0 = 330$ yr (August 2010) according to the same analysis (see text). **Panel (b):** Thermal luminosities L_γ in 10^{34} erg s^{-1}, calculated from the data shown in panel (a). The shaded area and errorbar illustrate 68% credible intervals of L_γ decline $s_L = 4s$ and $L_\gamma(t_0)$. **Panels (c) and (d):** Same as in panels (a) and (b) but for redshifted surface temperature $\widetilde{T}_{\rm s}$ and luminosity $\widetilde{L}_\gamma$.

below:

$$\widetilde{L}_\gamma = L_\gamma(1 - r_{\rm g}/R) = 4\pi\sigma_{\rm SB}\widetilde{T}_{\rm s}^4\widetilde{R}^2, \quad (3)$$

$$\widetilde{T}_{\rm s} = T_{\rm s}\sqrt{1 - r_{\rm g}/R}, \quad \widetilde{R} = R/\sqrt{1 - r_{\rm g}/R}, \quad (4)$$

where $r_{\rm g} = 2GM/c^2$ is the Schwarzschild radius and G is the Newtonian gravitational constant. As noted previously (Potekhin et al., 2020), estimates of redshifted quantities $\widetilde{T}_{\rm s}$ and $\widetilde{L}_\gamma$ can be more robust than of their non-redshifted counterparts $T_{\rm s}$ and L_γ. The estimates of $\widetilde{T}_{\rm s}$ and $\widetilde{L}_\gamma$ are shown in panels (c) and (d) of Fig. 1, analogous to panels (a) and (b) for $T_{\rm s}$ and L_γ. Errorbars for $\widetilde{T}_{\rm s}(t_0)$ and $\widetilde{L}_\gamma(t_0)$ take into account the estimates of M with their uncertainties from Shternin et al. (2023), in addition to the uncertainties in R and $T_{\rm s}$. The reported M and R estimates with their uncertainties give the gravitational redshifts

$$z_{\rm g} = (1 - r_{\rm g}/R)^{-1/2} - 1 \quad (5)$$

in the interval $z_{\rm g} \in [0.18, 0.34]$ (at 68% credibility). We see that using the redshifted quantities allows us to reduce the differences between model results (compare vertical scales in the left and right halves of Fig. 1).

The regression model for $\widetilde{L}_\gamma(t)$ in Fig. 1d reads

$$\log\widetilde{L}_\gamma(t) = \log\widetilde{L}_\gamma(t_0) - s_L\log(t/t_0), \quad (6)$$

where $\log\widetilde{L}_\gamma(t_0)\,[\mathrm{erg\ s^{-1}}] = 33.86\pm0.06$ and $s_L = 2.5\pm0.7$. The indicated $\log\widetilde{L}_\gamma(t_0)$ interval is twice larger than that of $\log L_\gamma(t_0)$ in Fig. 1c due to the NS mass uncertainty. It not only embraces the underlying results of Shternin et al. (2023), based on all ACIS data, but also covers all estimates obtained from separate Graded and Faint mode analyses (Wijngaarden et al., 2019; Posselt and Pavlov, 2022). Therefore we choose $\widetilde{L}_\gamma$ and Eq. (6) for comparison with cooling simulations.

3. Nucleon superfluidity

Superfluidity of neutrons and/or protons in NS interiors can strongly affect cooling of NSs. Each superfluidity is characterized by its own density-dependent critical temperature $T_{\rm crit}$. It can change the neutrino emissivity Q_ν, heat capacity c_V, and thermal conductivity $\varkappa$ of dense matter. In particular, it initiates the PBF process outlined in Section 1 but suppresses the rates of other neutrino emission processes. It can increase the heat capacity of nucleons at T slightly below $T_{\rm crit}$, but strongly suppress it at $T \ll T_{\rm crit}$. Superfluidity affects the thermal conductivity of nucleons by modifying nucleon-nucleon collision rates. It also affects the thermal conductivities of electrons and muons, because it changes screening of Coulomb interactions

in neutron-star matter as detailed in a comprehensive review by Schmitt and Shternin (2018).

Superfluidity is accompanied by the appearance of energy gaps Δ in distribution functions of strongly degenerate nucleons (neutrons and protons) in momentum (wavevector $\boldsymbol{k}$) space near respective Fermi surfaces ($k = k_{\rm Fn}$ and $k = k_{\rm Fp}$). Such gaps are calculated from integral equations which describe Cooper pairing of nucleons under attractive components of nuclear interactions in dense NS matter. Any gap Δ depends on a chosen EoS (on underlying model of nuclear interactions), on pairing channel, density ρ (usually parameterized by the values of $k_{\rm Fn}$ and $k_{\rm Fp}$), temperature T, and also on the direction of $\boldsymbol{k}$ on the Fermi surface. The zero-temperature gap $\Delta_0(k_{\rm F}) = \Delta(k_{\rm F}, T)$ is basic. Superfluidity occurs at those densities at which the gap equation gives $\Delta(k_{\rm F}, T) > 0$. At such densities the gap typically decreases with growing T and vanishes at $T = T_{\rm crit}(\rho)$. Some models predict the appearance of other particles (e.g. hyperons or quarks) in NS cores, which can also be in superfluid states, but we do not discuss them here, for simplicity.

As a rule, one considers three main channels of Cooper pairing of nucleons in NS interiors: neutron singlet (ns), proton singlet (ps), and neutron triplet (nt) ones. The first channel is effective for free neutrons in the inner crust, while the others operate mainly in the NS core.

In the case of singlet pairing the gap is isotropic, so that $\Delta(k_{\rm F}, T)$ is actually independent of the direction of $\boldsymbol{k}$. However, for triplet pairing the gap varies over the neutron Fermi surface. To be specific, let us focus on the $^3{\rm P}_2$ pairing or more complicated but similar $^3{\rm P}_2$–$^3{\rm F}_2$ pairing; they are most used in cooling calculations. Then the superfluid gap along the poles of Fermi surface appears to be about twice larger than along the equator, and it is customary (e.g., Takatsuka and Tamagaki 2004; Krotschek et al. 2024) to use the effective triplet gap $\Delta_{\rm eff,nt}(k_{\rm Fn}, T)$ as the rms value of $\Delta(k_{\rm Fn}, T)$ (over the Fermi surface). Its temperature dependence possesses the properties quite similar to those for the singlet pairing gap $\Delta_{\rm ns}(k_{\rm Fn}, T)$. We will refer to $\Delta_{\rm eff,nt}(k_{\rm Fn}, T)$ as to $\Delta_{\rm nt}(k_{\rm Fn}, T)$ for brevity.

Note some ambiguity to label $\Delta_{\rm nt}$ by different authors associated with presenting the $\boldsymbol{k}$-dependent gap by introducing specifically normalized gaps and angular functions (e.g., compare the notations in Amundsen and Østgaard 1985; Elgarøy et al. 1996a; Yakovlev et al. 1999, Takatsuka and Tamagaki 2004). A comment will be given further.

In the ideal case, for cooling simulations one needs the gaps $\Delta(k_{\rm F}, T)$ and respective modifications of microphysics (Q_ν, c_V, and κ) in superfluid matter, based on the same microscopic models. Such detailed and self-consistent data are not available yet.

Cooling simulations are usually performed for those EoSs, for which the gaps have not been studied. Then the gaps are taken from different EoSs. The majority of theorists calculate only zero-temperature gaps, $\Delta_0(k_{\rm F})$. Possible extensions to higher T have been discussed in the literature, but the results are sparse (e.g., Takatsuka and Tamagaki 2004; Ding et al. 2016; Krotschek et al. 2024). Nevertheless, it has been noted (e.g., Takatsuka and Tamagaki 2004; Krotschek et al. 2024) that a relation between $T_{\rm crit}$ and Δ_0 for quite different nuclear models stays close to the BCS relation (7) below. Also, the temperature dependence $\Delta(T/T_{\rm crit})/\Delta_0$ appears to be close to universal, although the universality can be violated at $T \approx T_{\rm crit}$ (Krotschek et al., 2024).

So far the majority of cooling simulations have been performed using sufficiently compact description of singlet and/or triplet proton-neutron superfluids based on Bardeen-Cooper-Schrieffer (BCS) models. As input parameters, one needs to know either the zero-temperature gap Δ_0 or the critical temperature $T_{\rm crit}$ for superfluidity of nucleons in a matter element. According to BCS, for singlet-state pairing, $T_{\rm crit}$ and Δ_0 are related as

$$k_{\rm B} T_{\rm crit} \approx 0.57\, \Delta_0, \tag{7}$$

where $k_{\rm B}$ is the Boltzmann constant. This relation (Bardeen et al., 1957) is universal and presented in many textbooks (e.g., Lifshitz and Pitaevskiĭ 1980). For triplet-state pairing the numerical coefficient is slightly different, but the difference seems to be not very important for cooling calculations.

The effects of superfluidity on Q_ν, c_V, and κ in the frame of the BCS theory have been calculated and described by analytic expressions as reviewed, e.g., by Yakovlev et al. (1999), Yakovlev et al. (2001), Potekhin et al. (2015), and Schmitt and Shternin (2018). In the NS cooling simulations presented below we calculate Q_ν, c_V, and $\varkappa$ following the review article by Potekhin et al. (2015) and the references therein.

We will parametrize the values of Δ_0 calculated for some EoSs as functions of Fermi wavenumbers of neutrons $k_{\rm Fn}$ and protons $k_{\rm Fp}$ in the form suggested by Kaminker et al. (2001),

$$\Delta_0(k_{\rm Fx}) = A_0\, \frac{(k_{\rm Fx} - k_0)^2}{(k_{\rm Fx} - k_0)^2 + k_1}\, \frac{(k_2 - k_{\rm Fx})^2}{(k_{\rm Fx} - k_2)^2 + k_3}, \tag{8}$$

if $k_0 < k_{\rm Fx} < k_2$, and $\Delta_0(k_{\rm Fx}) = 0$ otherwise; A_0 and k_i are fit parameters. A collection of these parameters was presented by Ho et al. (2015). In Table 1 we have reproduced some of them and added some new results. From now to the end of this section we outline the calculations of Δ_0 available in the literature and drop the subscript '0' for simplicity.

3.1. Neutron singlet pairing

Gandolfi et al. (2009) performed ab initio simulations of $\Delta_{\rm ns}$ in the range of $k_{\rm Fn}$ from 0.4 fm^{-1} to 1 fm^{-1}. As compared with the results of Margueron et al. (2008) (MSH), the corresponding parametrization GIPSF as a function of $k_{\rm Fn}$ has maximum by $\approx$ 20% higher at $k_{\rm Fn}$ that is $\approx$ 10% smaller. It has been checked that the difference between the MSH and GIPSF parametrizations is unimportant for thermal evolution of isolated NSs (Potekhin and Chabrier, 2018) and accreting NSs in soft X-ray transients (Potekhin et al., 2019; Potekhin and Chabrier, 2021). Ding et al. (2016) studied short- and long-range correlation effects on neutron pairing gaps, using effective nucleon interactions Av18, CDBonn, and Idaho. In all three cases, which we denote D16a, D16b, and D16c, respectively, they obtained $\Delta_{\rm ns}(k_{\rm Fn})$ close to one another and to MSH (Fig. 2a). They, however, noticeably differ from an older model SFB (Schwenk et al., 2003) shown in Fig. 2a by the long-dashed lines.

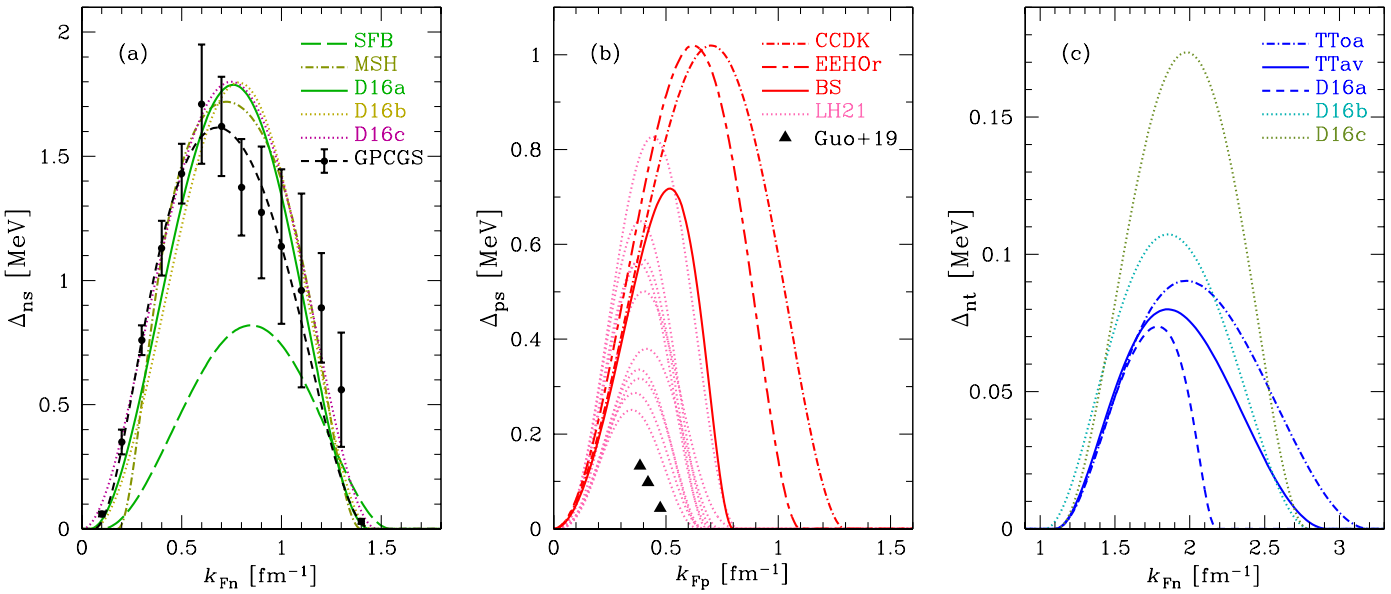

Figure 2: Superfluid gaps as functions of nucleon Fermi wavenumbers for superfluidity types ns (a), ps (b), and nt (c). Lines show analytical fits (8) according to the legend with the parameters listed in Table 1, except for the dotted lines in panel (b), which show the analytical fits of Lim and Holt (2021) (LH21) with the parameters listed in their Table II. Black dots with errorbars are numerical results of Gandolfi et al. (2022) (GPCGS in panel a) and black triangles refer to Guo et al. (2019) (Guo+19 in panel b).

Recently, Gandolfi et al. (2022) have published results of ab initio quantum Monte Carlo calculations of $\Delta_{ns}(k_{Fn})$ using realistic nuclear Hamiltonians that included two- and three-body interactions in an extended k_{Fn} range. In Fig. 2a these results are reproduced by dots with errorbars. Our best fit to them according to Eq. (8) is shown in the same figure by the short-dashed line; its parameters are listed in Table 1 (labeled as GPCGS). These results are consistent with the MSH and D16(a,b,c) parametrizations within $\lesssim 2$ errorbars, so that the difference between the latter parametrizations and GPCGS is not very significant. Below we mainly use the D16a parametrization of the ns pairing gap Δ_{ns} as a representative example.

3.2. Proton singlet pairing

Early models of the ps pairing gap Δ_{ps} predicted that it has a maximum $\sim$ 1 MeV and remains non-zero to rather large Fermi wavenumbers $k_{Fp} \gtrsim 1$ fm^{-1}. Examples are presented in Fig. 2b by the CCDK (Chen et al., 1993) and EEHOr (Elgarøy et al., 1996b) models. However, Baldo and Schulze (2007) have found that the allowance for three-body effective nuclear forces and in-medium effects (such as modified effective nucleon masses and polarization) reduces Δ_{ps} substantially. The red solid line in Fig. 2b shows the Baldo and Schulze's (hereinafter BS) model for Δ_{ps} as a function of Fermi wavenumber k_{Fp}, as parametrized by Ho et al. (2015). Moreover, Guo et al. (2019) argue that a proper account for density dependence of proton-proton induced interactions in NS matter leads to even stronger suppression of proton superfluidity. Their results are displayed by the triangles in Fig. 2b.

Lim and Holt (2021) studied proton pairing using chiral effective field theory and obtained a broad variety of gaps as functions of k_{Fp}. These gaps depend on details of theoretical models (choice of effective potentials, proton fraction in or out of β-equilibrium, order in chiral expansion, high-momentum cutoff). In any case they are either similar to or smaller than the BS gap, which confirms that the proton superfluidity is strongly suppressed. A representative set of the latter gap functions is displayed in Fig. 2b by dotted lines.

3.3. Neutron triplet pairing

The parametrizations TToa and TTav for the neutron $^3P_2$–$^3F_2$ pairing state are illustrated in Fig. 2c. They are constructed for reproducing critical temperatures T_{nt}, calculated by Takatsuka and Tamagaki (2004) using either their effective nucleon interaction potential OPEG-A or the potential Av18 (Wiringa et al., 1995), and supplemented by three-body effective potentials. Notice that the parameter A_0 in our Table 1 for superfluidity models TToa and TTav is approximately five times smaller than the analogous parameter in Ho et al. (2015). This is a result of the unfortunate ambiguity of labeling triplet gaps mentioned above. Ho et al. (2015) actually approximated not the gap but an artificially introduced gap amplitude. Nevertheless, they included the proper rescaling in the expression of T_{crit}. Their resulting values of T_{nt} are true and agree with figure 5 of Takatsuka and Tamagaki (2004). We present the values of A_0 obtained in the same way as for other models.

Ding et al. (2016) have also studied the effects of correlations for this type of pairing. The rising segments of $\Delta_{nt}(k_{Fn})$ curves are similar for all three models at the Fermi wave numbers $k_{Fn} \lesssim 1.8$ fm^{-1}, which correspond to $\rho \lesssim 3.5 \times 10^{14}$ g cm^{-3} for the BSk24 EoS (see Fig. 3). At larger k_{Fn} (larger ρ), the TTav curve $\Delta_{nt}(k_{Fn})$ bends downwards more rapidly than TToa, and the D16a curve decreases still faster than the TTav curve.

Table 1: Fit parameters in Eq. (8) for the pairing gap models shown in Fig. 2. Some listed parameters were obtained by Ho et al. (2015) by fitting the numerical results of Schwenk et al. (2003) (SFB), Margueron et al. (2008) (MSH), Chen et al. (1993) (CCDK), Elgarøy et al. (1996b) with relativistic corrections (EEHOr), Baldo and Schulze (2007) (BS), Takatsuka and Tamagaki (2004) for the OPEG-A or Av18 effective potentials (TToa and TTav, respectively; the corresponding values of A_0 are smaller than in Ho et al. 2015 because of different definitions of Δ_{nt}, see the text). For the ns and nt superfluidities, we also add the fit parameters obtained by Ding et al. (2016) by fitting their numerical results based on nucleon-nucleon potentials Av18 (D16a), CDBonn (D16b), and Idaho (D16c). The model GPCGS is our fit to the ns gap calculations by Gandolfi et al. (2022).

Gap model	A_0 (MeV)	k_0 (fm^{-1})	k_1 (fm^{-2})	k_2 (fm^{-1})	k_3 (fm^{-2})
Neutron singlet (ns)					
SFB	45	0.10	4.5	1.55	2.5
MSH	2.45	0.18	0.05	1.4	0.1
D16a	14.07	0.04	1.00	1.44	0.78
D16b	18.18	0.05	1.39	1.45	0.81
D16c	5.85	0.00	0.46	1.48	0.42
GPCGS	3.6	0.06	0.16	1.45	0.34
Proton singlet (ps)					
CCDK	102	0	9.0	1.3	1.5
EEHOr	61	0	6.0	1.1	0.6
BS	17	0	2.9	0.8	0.08
Neutron triplet (nt)					
TToa	0.44	1.1	0.60	3.2	2.4
TTav	0.63	1.1	0.60	2.92	3.0
D16a	0.17	1.1	0.35	2.18	0.05
D16b	0.41	1.03	0.56	2.81	1.00
D16c	0.60	1.11	0.69	2.79	0.53

Let us note that the D16a parametrization was obtained by Ding et al. (2016) neglecting three-nucleon forces (3NF). Preliminary results including 3NF forces, presented by these authors, show an increase of the triplet gap (unlike in singlet pairing case) and do not demonstrate the gap closure at large densities, and the D16a gap approaches the TTav gap (obtained with the same Av18 potential). The authors caution that at so high densities the applicability of their theory may be questionable.

Starting from the pioneering work by Tamagaki (1970), the $^3P_2$–$^3F_2$ pairing mode was deemed to be the dominant mode of the nt pairing. However, recently Krotscheck et al. (2023, 2024) went beyond conventional mean-field calculations by systematically summing large arrays of Feynman diagrams and obtained a radical suppression of the $^3P_2$–$^3F_2$ triplet pairing gap and an enhancement of the $^3P_0$ gap. It is also worth noting that Baldo et al. (1998) have found that the available nucleon-nucleon interaction potentials do not allow one to obtain reliable predictions for the $^3P_2$–$^3F_2$ gap at densities above $\sim 1.7\rho_0$, where ρ_0 is the saturation density for symmetric nuclear matter. Thus the theoretical predictions for the nt superfluidity remain highly uncertain.

3.4. Critical temperatures

Fig. 3 displays T_{crit} as a function of mass density ρ in the NS interior for some of the models listed in Table 1 and illustrated in Fig. 2. Here, we show only those models that are employed in our cooling calculations discussed in Section 4 below. To relate the Fermi wavenumbers to the mass density, we have adopted the EoS and composition of the NS matter given by the BSk24 model (Pearson et al., 2018). Note that the employed model predicts an appearance of free protons in a narrow density interval inside the inner crust, adjacent to the crust-core boundary at density ρ_{cc}, which gives rise to the rapid but continuous increase of the critical temperature T_{ps} in this interval. Consequently, the red curves in Fig. 3 only change their slope, but are continuous at $\rho = \rho_{cc}$, unlike the more common older models, which assumed an abrupt disappearance of the free protons with decreasing density and, therefore, an abrupt vanishing of the corresponding lines at $\rho < \rho_{cc}$. This figure demonstrates that the ns pairing is well developed in almost the entire inner crust of NSs at temperatures $T \ll 10^{10}$ K, but there are large uncertainties concerning the ps and nt superfluidities in the core: depending on the model, they can either spread over the entire core down to the NS center at $\rho = \rho_{cen}$ or vanish at much lower densities, leaving a large part of the core nonsuperfluid.

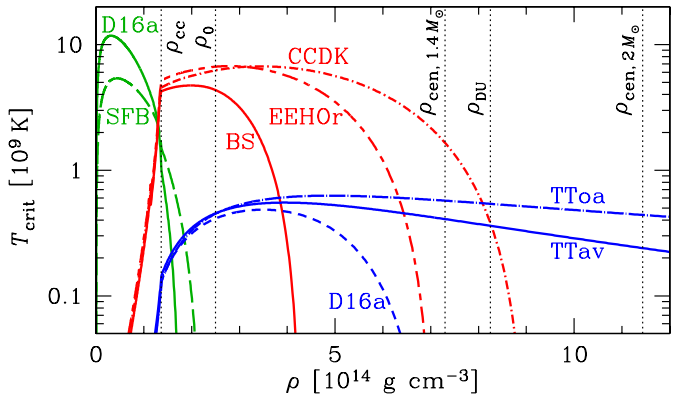

Figure 3: Critical temperatures for superfluid phase transition T_{crit} versus mass density for the BSk24 EoS and various superfluidity models. Green, red and blue curves show $T_{crit} = T_{ns}$, T_{ps}, and T_{nt}, respectively, for ns, ps, and nt pairing channels, according to the models listed in Table 1. Triangles display T_{ps} according to Guo et al. (2019). Vertical dotted lines mark the crust-core boundary ρ_{cc}, nuclear saturation $\rho_0 \approx 2.5\times10^{14}$ g cm^{-3} (Horowitz et al., 2020), direct Urca threshold ρ_{DU}, and central densities ρ_{cen} of NSs with $M = 1.4\,M_\odot$ and $2.0\,M_\odot$.

4. Cooling simulations compared with the observations

To simulate NS cooling, we use our numerical code described in Potekhin and Chabrier (2018). The physics input is mainly the same as reviewed in Potekhin et al. (2015), but it incorporates also the enhancement of mUrca reaction rates near dUrca thresholds as suggested by Shternin, Baldo, and Haensel (2018, hereafter SBH).

4.1. PBF scenario

We start with the combination of NS parameters similar to the best-fit solution found for the Cas A NS by Ho et al. (2015). They employed a version of the NS cooling code (Gnedin et al., 2001) with $q_{PBF} = 0.76$ and tried different superfluidity and EoS models, envelope compositions, and NS masses. Their best-fit

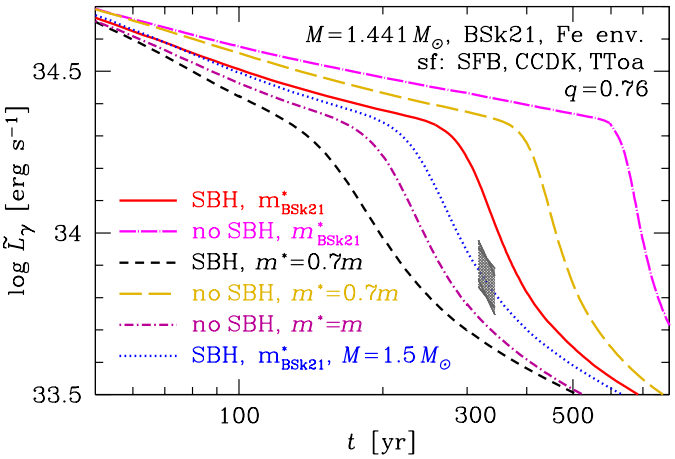

Figure 4: Cooling curves (redshifted luminosity $\widetilde{L}_\gamma$ versus age t) in logarithmic scale for the best-fit case of Ho et al. (2015): $M = 1.441\,M_\odot$, BSk21 EoS with ns, ps, and nt superfluidities SFB, CCDK, and TToa, respectively; the heat blanketing envelope composed of heavy elements (pure iron or ground state compositions); the PBF efficiency factor is $q_{\rm PBF} = 0.76$. The curves differ by microphysics inputs: either including the SBH enhancement of mUrca processes (solid and short-dashed lines) or excluding it (one long-dashed and two dot-dashed lines), using either the EoS-consistent effective nucleon masses $m^*_{\rm BSk21}$ (solid and dot–long-dash lines) or fixed ratios m^*/m with respect to bare nucleon masses m in the NS core (one dot–short-dash and two dashed lines). In addition, the dotted curve is obtained with the same microphysics as the solid one, but at $M = 1.5\,M_\odot$. The gray shaded area corresponds to the slopes and errorbar from Fig. 1d.

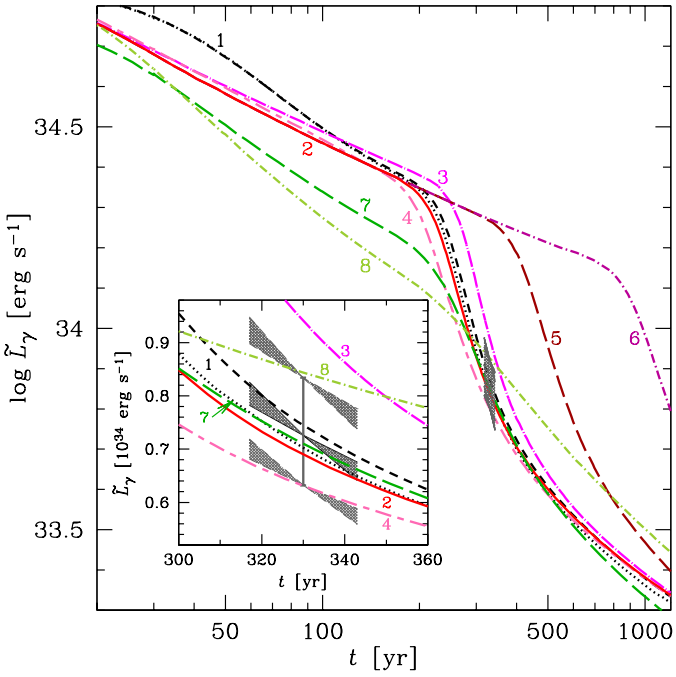

Figure 5: NS cooling curves simulated with $q_{\rm PBF} = 0.76$, ground-state blanketing envelope, and different EoS and superfluidity models according to Table 2. The gray shaded area in the main panel is the same as in Fig. 4. The inset shows segments of the cooling curves in linear scale around the age and luminosity of the Cas A NS. The vertical bar plots the 1σ confidence interval for $\widetilde{L}_\gamma$, while the central shaded area shows the 1σ slope range s_L; it is centered at the best-fit $\widetilde{L}_\gamma$ value according to the results of Section 2. The upper and lower shaded areas show similar regions shifted up and down to the ends of the vertical bar.

solution is characterized by $M = 1.441 M_\odot$, the BSk21 EoS (Potekhin et al., 2013), strong proton singlet (ps) superfluidity CCDK (Chen et al., 1993), moderate neutron triplet (nt) superfluidity TToa (Takatsuka and Tamagaki, 2004), relatively weak neutron singlet (ns) superfluidity SFB (Schwenk et al., 2003), and a heat blanket made of iron. The latter implied that the outermost carbon layer is sufficiently thin to be insignificant for heat transport, but sufficiently thick to validate the use of the carbon atmosphere model for fitting the observed spectra. Corresponding NS cooling is illustrated in Fig. 4. The gray shaded area meets 1σ ranges of the slopes and absolute values for $\log \widetilde{L}_\gamma$ according to Section 2. Fig. 4 does not reproduce the results of Ho et al. (2015) exactly (e.g., their Fig. 14), because we use the updated observational results (Shternin et al., 2023) and show redshifted luminosity $\widetilde{L}_\gamma$ (instead of $T_{\rm s}$).

We have explored the effects of various physics updates in our cooling code on matching the Cas A NS observations. The strongest effects are produced by effective masses of nucleons, which we adjust to a specific EoS,[1] and by the SBH enhancement of mUrca reactions due to in-medium effects. In Fig. 4 we show cooling curves for the best-fit global NS parameters of Ho et al. (2015), using the PBF efficiency factor $q_{\rm PBF} = 0.76$ but varying other microphysics details. We consider the models either with or without the SBH effect and either with EoS-consistent effective masses or with constant m^* in the NS core, like in the cooling code employed by Ho et al. (2015). Other improvements, realized in our cooling code, have minor effects on cooling curves at the Cas A NS age. They include updated neutrino emission due to plasmon decay (Kantor and Gusakov, 2009), more detailed ground state composition of the outer crust and its accurate time-dependent thermal structure, instead of employing fits for quasi-stationary pure iron outer crust. Also, we have improved radiative opacities in atmospheric layers by including electron-positron pairs at high temperatures (Potekhin and Chabrier, 2018).

The dotted curve in Fig. 4 is obtained with the same model as the solid one, but for $M = 1.5\,M_\odot$ instead of $1.441\,M_\odot$. It demonstrates that in some cases the cooling curves can be adjusted to the observed $\widetilde{L}_\gamma$-range by varying M.

The BSk21 EoS was upgraded to BSk24 by Pearson et al. (2018). The upgrade consisted in using the parameters of an effective nucleon-nucleon interaction potential adjusted by Goriely et al. (2013) for reproducing the most recent experimental nuclear mass data (Wang et al., 2012). The effect of this update on cooling curves is minor: it is illustrated by the two curves near label 1 in Fig. 5, where the dotted curve is the same as in Fig. 4 and the dashed one is obtained by replacing the BSk21 EoS with BSk24.

The parameters for cooling curves in Fig. 5 are listed in Table 2. Simulation No. 2 differs from No. 1 by using another neutron singlet superfluidity, D16a (Ding et al., 2016), instead of SFB (Fig. 3). Its zero-temperature gap reaches maximum

[1] The effective masses enter our calculations through the expressions for neutrino emission rates, nucleon heat capacities, and neutron thermal conductivity, but the superfluid gaps described in Section 3 are kept intact (introducing thus an insignificant inconsistency).

Table 2: NS parameters for cooling curves in Fig. 5: EoS (column 2), NS mass M in units of $M_\odot$ (column 3), and superfluidity models for neutron singlet (ns), proton singlet (ps), and neutron triplet (nt) pairing channels (columns 4, 5 and 6, respectively) according to analytical approximations exposed in Section 3: SFB or D16a for the ns pairing type, CCDK or EEHOr for the ps pairing, and TToa, TTav, or D16a for the nt pairing.

			Superfluidity models		
No.	EoS	$M\,[M_\odot]$	ns	ps	nt
1	BSk21/24	1.50	SFB	CCDK	TToa
2	BSk24	1.50	D16a	CCDK	TToa
3	BSk25	1.50	D16a	CCDK	TToa
4	BSk25	1.55	D16a	CCDK	TToa
5	BSk24	1.50	D16a	CCDK	TTav
6	BSk24	1.50	D16a	CCDK	D16a
7	BSk24	1.30	D16a	EEHOr	TTav
8	BSk24	1.55	D16a	EEHOr	D16a

of $\approx 1.7 \pm 0.2$ MeV (corresponding to the critical temperature $T_{\rm ns} = (1.12 \pm 0.13) \times 10^{10}$ K) at the Fermi wave number of neutrons $k_{\rm Fn} \approx 0.7$ fm^{-1}, and it vanishes at $k_{\rm Fn} \gtrsim 1.4$ fm^{-1}. For comparison, the SFB gap has nearly twice lower maximum.

The limiting wave number of the ns superfluidity, $k_{\rm Fn} \approx 1.4$ fm^{-1}, corresponds to the number density of neutrons $n_{\rm n} \approx 0.09$ fm^{-3}, which is close to the nucleon number density at the NS crust-core interface. Accordingly, this superfluidity is important in the crust but not in the core. For that reason, curve 2 in Fig. 5 is similar to curves 1 at the Cas A NS age $t \gtrsim 300$ yr, when the thermal relaxation of the crust is already over. Nevertheless, there is an appreciable difference between these curves at $t \lesssim 100$ yr, when the thermal relaxation of the crust is not finished yet.

Curve 3 in Fig. 5 differs from curve 2 by using a stiffer BSk25 EoS from Pearson et al. (2018), characterized by a smaller assumed nuclear symmetry energy at the nuclear saturation density (29 MeV instead of 30 MeV). Curve 4 differs from curve 3 by a slightly larger assumed NS mass, $M = 1.55\,M_\odot$.

Curves 5 and 6 in Fig. 5 differ from curve 2 by the adopted models for neutron pairing gap $\Delta_{\rm nt}$ in the NS core, TTav and D16a, instead of TToa. Since the TTav and D16a curves $T_{\rm nt}(\rho)$ bend downwards at large ρ more rapidly than TToa (Fig. 3), the development of the PBF process is delayed for the TTav superfluidity till the core cools to a lower temperature than for the TToa, and to a still lower temperature in the D16a case. This explains the shift of the steep decline of curves 5 and 6 to later ages t compared to curve 2.

The retardation of cooling curves 5 and 6 can be compensated by reducing proton superfluidity. Replacing strong CCDK ps superfluidity by EEHOr, which has a quicker decline of $T_{\rm ps}(\rho)$ with increasing density (see Fig. 3), we obtain even too fast cooling at early ages for the TTav nt superfluidity. The corresponding cooling curve can be further tuned by decreasing the NS mass to $1.3\,M_\odot$ (curve 7). For weaker D16a neutron superfluidity, the weaker proton superfluidity EEHOr should be supplemented by a small increase of M to match the allowed range for the Cas A NS, as illustrated by curve 8. However, the slope of this curve is too small compared with the observations.

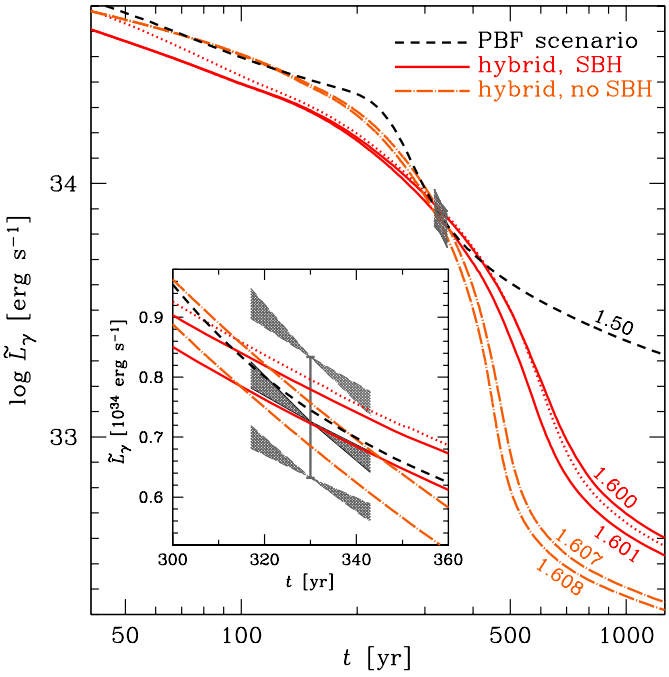

Figure 6: NS cooling curves simulated with the PBF efficiency parameter $q_{\rm PBF} = 0.19$, CCDK and TToa parametrizations for ps and nt superfluidities in the NS core, BSk24 EoS, heavy-element heat-blanketing envelope, and different $M/M_\odot$ marked near the curves. The solid and dot-dashed cooling curves are simulated with or without the SBH effect, respectively, using the D16a ns superfluidity in the inner crust. For comparison, the dotted curve shows the same as the upper solid curve, but with the SFB model for the ns superfluidity in the crust, and the dashed curve reproduces case 1 from Fig. 5, with larger $q_{\rm PBF} = 0.76$ and smaller $M/M_\odot = 1.5$. The inset shows segments of cooling curves in linear scale in the current epoch. The vertical bar and shaded areas are the same as in Fig. 5.

This means that the nt superfluidity D16a is too weak to provide the required PBF neutrino luminosity.

As argued above, contemporary theory predicts that proton superfluidity is likely weaker than in the BS model, which is still weaker than EEHOr and vanishes in a central part of the NS core. Since a weak proton superfluidity cannot strongly delay early cooling, PBF processes begin to operate much earlier than the current Cas A NS age and cannot explain the data (see Section 4.3).

4.2. *Hybrid scenario*

In Section 4.1 we have tested the PBF efficiency factor $q_{\rm PBF} = 0.76$ consistent with Leinson and Pérez (2006). As mentioned in Section 1, the corrected value $q_{\rm PBF} = 0.19$ by Leinson (2010) is too small to match Cas A NS observations in the PBF cooling scenario. To reconcile the apparent cooling rate with the theory, Leinson (2022) proposed the hybrid cooling scenario, where the PBF process is supplemented by dUrca, together providing the desired cooling rate. Following Ho et al. (2015), he used the SFB and TToa parametrizations for the critical temperatures $T_{\rm ns}$ and $T_{\rm nt}$, the strong proton superfluidity model CCDK, and the heat blanketing envelope composed of iron. He performed NS cooling simulations using the BSk24 EoS and found that the simulated cooling agrees with the ob-

served one for the Cas A NS, if the NS mass ($M = 1.6\,M_\odot$) slightly exceeds the dUrca threshold value $M_{\rm DU} = 1.595\,M_\odot$.

Our simulated cooling curve with the same model parameters is displayed in Fig. 6 by dots. Replacing the SFB model for $T_{\rm ns}$ by D16a has a negligible effect at the Cas A NS age, which is demonstrated in Fig. 6 by the upper solid curve (in analogy with the same replacement in Fig. 5). The increase of M from $1.600\,M_\odot$ to $1.601\,M_\odot$ causes a stronger effect, illustrated in Fig. 6 by the lower solid curve. While these curves have the same slope at $t = t_0$, as the cooling curve in the PBF scenario with $q_{\rm PBF} = 0.76$ (the dashed curve), and are compatible with the observations at the edge of the 1σ confidence interval, they still demonstrate a noticeably slower decline and worse agreement with the observations than it was found by Leinson (2022). This difference is likely caused by the absence of the SBH effect (Shternin et al., 2018) in the public cooling code NScool (Page, 2016) employed by Leinson (2022). By switching the SBH effect off we are able to perfectly reproduce the Leinson's best-fit cooling rate for the Cas A NS, as illustrated in Fig. 6 by dot-dashed lines.

Recently, Tu and Li (2025) have considered the same scenario using other EoS models, which allowed dUrca processes with hyperons. These authors have obtained similar results and derived constraints on $T_{\rm nt}$ relevant to the PBF and hybrid scenarios from the condition that the enhanced PBF cooling develops at the Cas A NS age.

4.3. Urca scenario

In the PBF scenario (Section 4.1) and the hybrid scenario (Section 4.2), in agreement with previous works, a strong proton superfluidity is required to slow down early cooling to delay the onset of neutron superfluidity (accompanied by the enhanced PBF cooling) until nearly the Cas A NS age. However, such a strong proton superfluidity is disfavored by modern theory (see Section 1). Besides, the heavy-element heat-blanketing envelope was needed in both scenarios to match the observed luminosity of the Cas A NS at its age, because the strong proton superfluidity slows down the cooling. For instance, according to Ho et al. (2015), the carbon layer, if present, should be extremely thin (to have the mass $M_{\rm C} \ll 10^{-11} M_\odot$) to match the observations.

Now we turn to an alternative Urca cooling scenario, which can be consistent with low PBF efficiency, weak proton superfluidity, and carbon envelope.

Fig. 7 shows cooling curves, simulated using our fiducial set of pairing gaps: D16a, BS, and TTav for the ns, ps, and nt superfluidities, respectively. Solid curves are calculated using the BSk24 EoS, the PBF efficiency factor $q_{\rm PBF} = 0.19$, the heat-blanketing envelope composed of carbon up to the largest densities and temperatures determined by the ignition line (as fitted in Potekhin and Chabrier, 2012) and composed of heavy elements beyond it (according to the ground state model of Pearson et al., 2018). Two NS masses, $M = 1.605\,M_\odot$ and $1.608\,M_\odot$, are selected, which fit the upper and lower ends of 1σ confidence interval for the observed thermal luminosity $\widetilde{L}_\gamma$. The star radius for this mass, EoS, and envelope composition is $R \approx 12.7$ km. Such M and R are consistent with

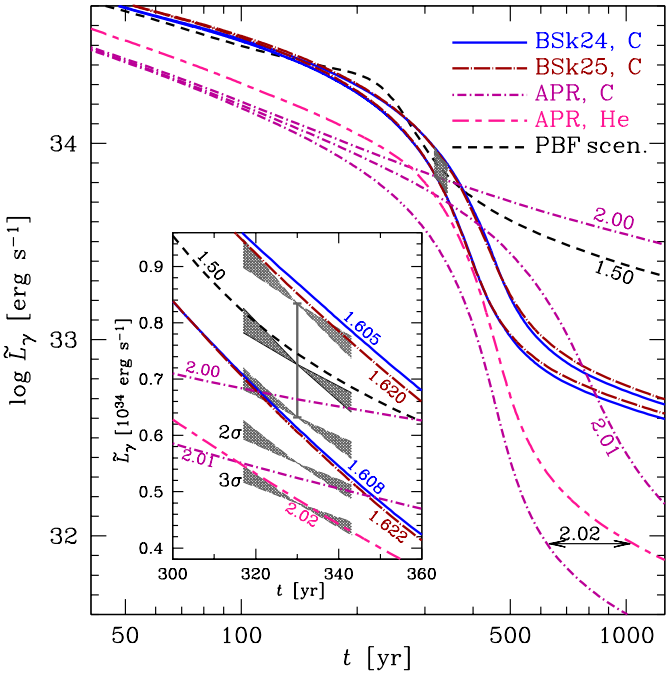

Figure 7: NS cooling curves simulated with the PBF efficiency factor $q_{\rm PBF} = 0.19$, superfluidity parametrizations D16a (ns), BS (ps), and TTav (nt), different EoSs and heat-blanketing envelopes according to the legend, and different $M/M_\odot$ marked near the curves. For comparison, as in Fig. 6, the dashed curve reproduces the PBF cooling curve 1 from Fig. 5. The gray shaded area in the main panel is the same as in Fig. 4. The inset shows segments of cooling curves in linear scale around the age and luminosity of the Cas A NS. Here, the vertical bar and the shaded area at its center are the same as in Fig. 1d. Also, displaced shaded areas covering the same range of the slope s_L in Eq. (6) are shown at ends of the bar $\widetilde{L}_\gamma(t_0) = 10^{33.86\pm0.06} \approx (0.63-0.83)\times10^{34}$ erg s^{-1} and at lower central values $\widetilde{L}_\gamma(t_0) = 10^{33.74} \approx 0.55\times10^{44}$ erg s^{-1} and $10^{33.68} \approx 0.48\times10^{44}$ erg s^{-1} (as 2σ and 3σ displacements of $\log\widetilde{L}_\gamma$, respectively).

$M = 1.55 \pm 0.15\,M_\odot$ and $R = 13.5 \pm 1.5$ km derived from observations (Shternin et al., 2023). The slope of simulated cooling curves $s_L = -{\rm d}\log\widetilde{L}_\gamma/{\rm d}\log t$ at $t = 330$ yr varies from 2.5 for $M = 1.605\,M_\odot$ to 3.7 for $M = 1.608\,M_\odot$ (to be compared with $s_L = 2.5 \pm 0.7$, derived from observations, see Section 2).

For comparison, the dashed curve in Fig. 7 reproduces cooling curve 1 from Fig. 5 obtained in the PBF scenario with $q_{\rm PBF} = 0.76$. In this case, the observations would require a stronger proton superconductivity (CCDK) and iron heat-blanketing envelope.

Dot–long-dash lines in Fig. 7 are analogous to solid ones, but for the stiffer BSk25 EoS. This yields the NS mass range $(1.620\,M_\odot, 1.622\,M_\odot)$ matching 1σ uncertainties in $\widetilde{L}_\gamma(t_0)$, which gives $R \approx 13.7$ km and $s_L(t_0) \in (2.6, 3.9)$.

Dot-short-dash cooling curves in Fig. 7 are calculated using a softer APR EoS (denoted as A18+δv+UIX* by Akmal et al. 1998). We use its parametrized form (Potekhin and Chabrier, 2018), which includes the NS crust described by the BSk24 EoS on top of the APR core. The best-fit luminosity is provided at $M = 2\,M_\odot$ (with $R = 11$ km), but the simulated slope $s_L(t_0) = 0.7$ is significantly lower than the one derived from observations. The mass increase allows us to reproduce the observed slope, but at much lower luminosity. The cooling curve

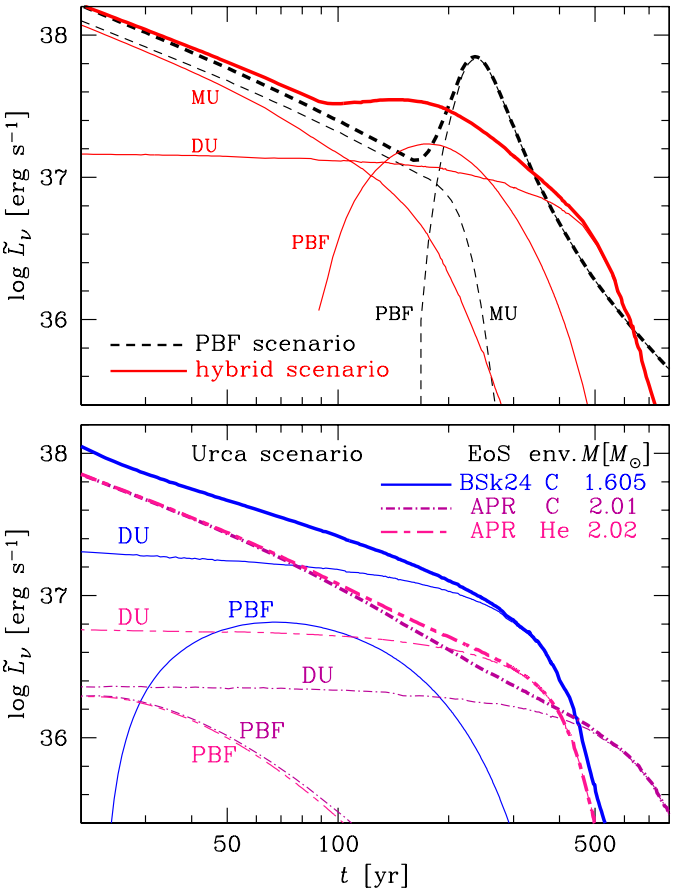

Figure 8: Neutrino luminosities in the NS core versus NS age. Thick lines show total redshifted neutrino luminosity; thin lines are partial luminosities due to the mUrca (marked MU, shown in the upper panel only), dUrca (DU), and PBF processes. *Upper panel:* The PBF and hybrid cooling scenarios. The dashed and solid lines correspond to the dashed line and the upper solid line in Fig. 6, respectively. *Lower panel:* The Urca cooling scenario. The solid, dot-dashed, and short-dash–long-dash lines correspond to the lines of the same types as in Fig. 7 for $M = 1.605\,M_\odot$, $2.01\,M_\odot$, and $2.02\,M_\odot$, respectively.

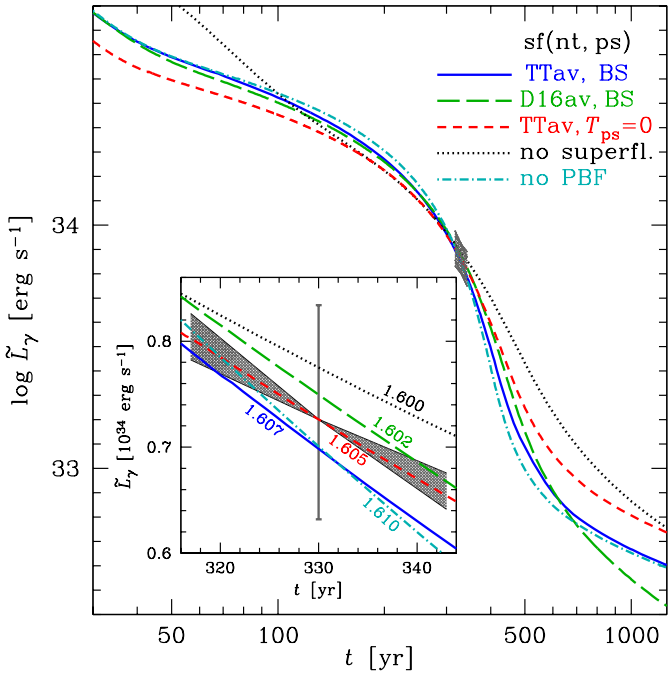

Figure 9: NS cooling curves simulated with $q_{\rm PBF} = 0.19$, BSk24 EoS and carbon heat-blanketing envelope at $M/M_\odot$ marked near the curves in the inset. Different line types correspond to different superfluidity models according to the legend (see the text). The shaded area in the main window is the same as in Figs. 4, 5, 6, and 7. The inset shows a zoom to the current ages and luminosities, with the errorbar and shaded area from Fig. 1d.

for $M = 2.01\,M_\odot$ has the slope near the lower end of the 1σ confidence interval and $L_\gamma(t_0)$ below the end of the 2σ interval, while the curve for $M = 2.02\,M_\odot$ has nearly best-fit slope, but unacceptably low luminosity at the Cas A NS age. One can partially alleviate the latter discrepancy by applying more heat-transparent envelope model. This is illustrated in Fig. 7 by the cooling curve for an NS with $M = 2.02\,M_\odot$ and heat-blanketing envelope composed of helium, but such an envelope is difficult to reconcile with the carbon atmosphere.

Large slopes of cooling curves in Figs. 6 and 7 occur for NS masses slightly exceeding the threshold mass $M_{\rm DU}$ for opening the dUrca process ($1.595\,M_\odot$, $1.612\,M_\odot$, and $2.005\,M_\odot$ in cases of BSk24, BSk25, and APR EoSs, respectively). In these cases, the dUrca cooling is not too strong, which allows the star to maintain a rather high luminosity in a few hundred years.

Time dependence of different neutrino cooling mechanisms is shown in Fig. 8. The figure displays total and partial neutrino luminosities $\widetilde{L}_\nu$ integrated over proper volume of the NS core with account for gravitational redshifts (see Glen and Sutherland, 1980). The upper panel shows the total and partial mUrca, PBF, and dUrca contributions for the PBF and hybrid cooling scenarios. Two models from Fig. 6 are selected for illustration. In the PBF scenario with $q_{\rm PBF} = 0.76$, the cooling is dominated by the mUrca processes at $t \lesssim 200$ yr and by the powerful PBF mechanism at later times. In the hybrid scenario with $q_{\rm PBF} = 0.19$, the PBF and dUrca mechanisms give comparable contributions at $t \sim 200$–300 yr.

The lower panel of Fig. 8 shows the PBF and dUrca neutrino luminosities for three models from Fig. 7 with a weaker proton superfluidity. In these cases, the PBF cooling rate reaches maximum at $t \lesssim 100$ yr and vanishes by $t \sim t_0$. The cooling is mostly provided by the mUrca and dUrca mechanisms; the former dominates at $t \lesssim 100$–200 yr and the latter at $t \gtrsim 200$–400 yr.

In Fig. 9 we primarily compare cooling curves for different NS superfluidity models in the Urca cooling scenario. We assume the BSk24 EoS and carbon envelope and adjust the NS mass for reproducing the Cas A NS redshifted photon luminosity within 1σ uncertainty. The solid and dashed cooling curves are obtained assuming the D16a neutron superfluidity in the crust but different models of nucleon superfluidities in the core. The solid curve shows NS cooling with the TTav and BS models for the nt and ps superfluidities, respectively, analogous to the solid curves in Fig. 7. The long-dashed curve is obtained for a weaker neutron superfluidity. The short-dashed curve is calculated without proton superfluidity, to test the effect of strong suppression of this superfluidity, suggested by some

modern theoretical results (see Section 1). For comparison, the dotted curve is calculated for a fully non-superfluid NS.

The slopes of the solid, long-dashed, short-dashed, and dotted cooling curves in Fig. 9 at $t = t_0$ are, respectively, $s_L(t_0) = 3.3$, 2.9, 2.6, and 2.1, in acceptable agreement with $s_L = 2.5 \pm 0.7$ derived from observations. The best agreement is provided assuming moderately weak neutron superfluidity TTav and strongly suppressed proton superfluidity, although the preference for this combination of superfluidities is not statistically significant.

Finally, the dot-dashed cooling curve in Fig. 9 is calculated with the same model as the solid curve, but neglecting the PBF contribution ($q_{\rm PBF} = 0$). It has a steeper slope $s_L(t_0) = 3.8$. Together with the results discussed above (see Fig. 7), this evinces an anticorrelation between $q_{\rm PBF}$ and $s_L(t_0)$ (as long as $\widetilde{L}_\gamma(t_0)$ stays within the observational limits) and confirms that the PBF mechanism is not needed for explaining rapid cooling of the Cas A NS.

It is important to stress the necessity of *tuning the Cas A NS mass M* to be consistent with the observations. Such a tuning is equivalent to tuning the dUrca kernel radius $r_{\rm D}$. According to our calculations (e.g., Fig. 10), the radius $r_{\rm D}$ should be $\sim$ 0.7–1.5 km, which corresponds to the mass M higher by $\sim$ 0.0015–0.015 $M_\odot$ than a critical mass $M_{\rm DU}$ for the onset of dUrca process in the stellar center. This delays the cooling in such a way to reach the observed enhanced cooling of the Cas A NS just in our epoch. Higher $M - M_{\rm DU}$ (or higher $r_{\rm D}$) would give even more enhanced cooling but it will end too early, making the Cas A NS colder than it is now. Lower $M - M_{\rm DU}$ (or $r_{\rm D}$) would prolong the delay to later epochs, making the Cas A NS too hot at present times and strongly reducing the enhancement.

Figure 10 reveals *three main cooling stages*. At the *first stage*, which typically lasts for few weeks after the NS birth, the dUrca kernel cools much faster than the surrounding core. This cooling is local: thermal coupling between the cold dUrca kernel and the outer core is still negligible. An efficient thermal quasi-stationary coupling occurs at the *second cooling stage* at which the kernel temperature is maintained nearly constant by a quasi-stationary balance between the neutrino outflow from the dUrca kernel and heat flow into it from the outer core. Initially, the neutrino cooling is mainly determined by mUrca processes in the outer core but later the heat flow into the cold kernel becomes dominant. At the *third cooling stage* the kernel and outer core thermally equilibrate, and the dUrca neutrino emission from the kernel controls the entire core cooling.

Fig. 11 illustrates radial distributions of neutrino emissivities due to mUrca and dUrca processes at different NS ages. We see that the mUrca emissivity is nearly constant in a wide layer of the outer core at ages $t \lesssim 1$ kyr. In addition, the dUrca emissivity varies relatively weakly at 1 yr $\lesssim t \lesssim$ 300 yr. We will use these features to construct an analytic toy model of NS cooling in the next section.

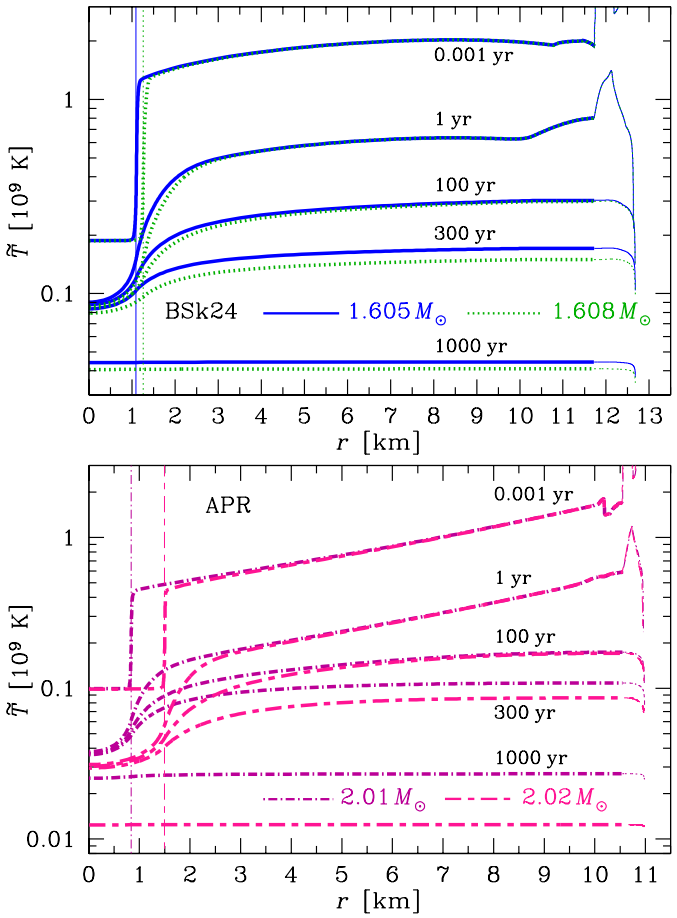

Figure 10: Snapshots of redshifted temperature profiles in the interior of some of the NS models employed in Fig. 7 at ages (from upper to lower curves of the same style) $t = 10^{-3}$ yr, 1 yr, 100 yr, 300 yr, and 1000 yr. The upper and lower panels refer to the structure of NSs with the EoS models BSk24 and APR, respectively. The solid, dot-dashed, and long-dash–short-dash curves correspond to the same NS models as the corresponding line styles in Fig. 7, with $M = 1.605\,M_\odot$ for the BSk24 EoS in the upper panel, as well as with $2.01\,M_\odot$ and $2.02\,M_\odot$ in the lower panel. The dotted curves in the upper panel correspond to the BSk24 EoS with $M = 1.608\,M_\odot$ (as the lower solid line in Fig. 7). The thick parts of the curves trace the core and the thin segments correspond to the crust. The thin vertical lines mark the boundary of the dUrca kernels.

5. Analytic model

5.1. Model outline

For clarifying the Urca cooling with a non-isothermal NS core, let us consider a toy model. We neglect superfluidity and General Relativity effects, simplify the dependencies of neutrino emissivities, heat capacity, and thermal conductivity on T, neglect their density dependence at constant T, and separate the cooling in several stages by retaining only the leading heat loss mechanism at each stage. Furthermore, we mainly treat the dUrca kernel and the outside core (the outer core) as isothermal, with generally different temperatures. The heat flux between them is meant to be controlled by a thin transition layer at $r = r_{\rm D}$.

The neutrino emissivity in the dUrca kernel can be approximated as $Q_{\rm D} = Q_{\rm D0}T^6$, the mUrca emissivity as $Q_{\rm M} = Q_{\rm M0}T^8$,

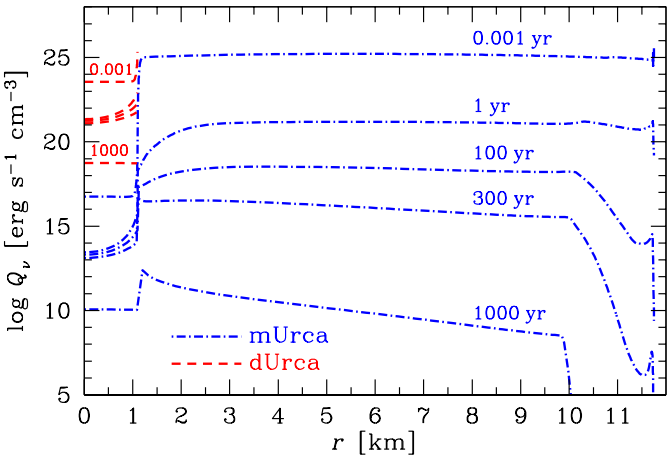

Figure 11: Neutrino emissivities due to mUrca (blue dot-dashed curves) and dUrca (red dashed curves) processes at different NS ages (marked near the curves) for the NS model with $M = 1.605\,M_\odot$, whose $\overline{T}(r)$ profiles are shown by solid lines in the upper panel of Fig. 10.

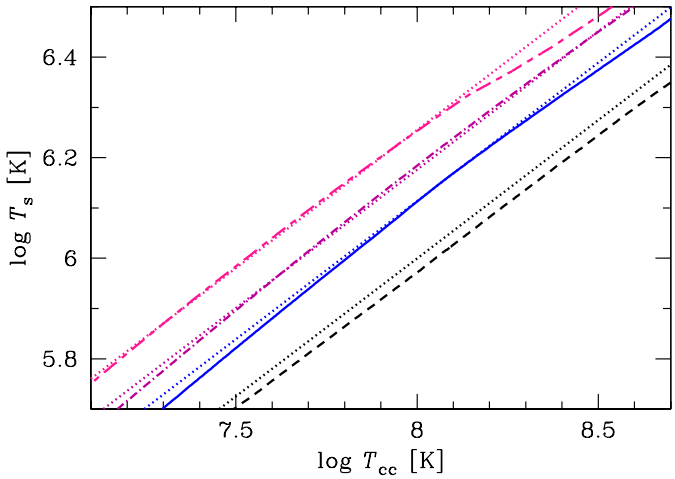

Figure 12: Effective surface temperature T_s as a function of the temperature T_{cc} at the crust-core interface in logarithmic scales. The dashed, solid, dot-dashed, and short-dash–long-dash lines correspond to the NS cooling models plotted by the same line types in Fig. 7. The dotted lines display the power-law (13) with $\beta_{cc} = 0.55$ and scaling parameters (from lower to upper lines) $T_{s0} = 1$ MK, 1.3 MK, 1.5 MK, and 1.8 MK.

the heat capacity per unit volume as $c_V = c_0 T$, and the thermal conductivity as $\varkappa = \varkappa_0/T$ (see, e.g., Potekhin et al., 2015). For quantitative estimates, we write

$$Q_D = 10^{21} g_D T_8^6 \text{ erg cm}^{-3} \text{ s}^{-1}, \quad (9)$$

$$Q_M = 10^{14} g_M T_8^8 \text{ erg cm}^{-3} \text{ s}^{-1}, \quad (10)$$

$$c_V = 3 \times 10^{19} g_c T_8 \text{ erg cm}^{-3} \text{ K}^{-1}, \quad (11)$$

$$\varkappa = 10^{23} g_\varkappa T_8^{-1} \text{ erg cm}^{-1} \text{ s}^{-1} \text{ K}^{-1}, \quad (12)$$

where $T_8 \equiv T/(10^8 \text{ K})$, while g_D, g_M, g_c and $g_\varkappa$ are correction factors of the order of unity. These factors are helpful for estimating scatter of possible values. For the EoSs and NS masses used in Fig. 10, we numerically obtain $g_M \approx 0.3$–5 in the outer part of the core (where the SBH enhancement is not too large), $g_D \approx 0.5$–3, $g_c \approx 0.6$–1.7, and $g_\varkappa$ varying from ~ 0.1–0.3 near the core boundary to $\sim$ 1–5 near the star center. The scatter in these factors is mainly determined by variations of the effective masses of the nucleons; for instance, $g_D \propto m_n^* m_p^*$ and $g_M \propto (m_n^*)^2$. As mentioned above, we neglect the density dependence of Q_{D0}, Q_{M0}, c_0, $\varkappa_0$ and treat them as constants.

In accordance with Section 4.3, we distinguish three main neutrino cooling stages, which we discuss below in more detail.

The first cooling stage is *local*, meaning that each volume element loses heat primarily directly (via neutrino emission), while conductive heat transport is negligible. This stage is much shorter than the NS ages we are interested in, but it creates the initial temperature profile for subsequent stages (Section 5.2).

At *the second* stage, the central temperature T_{cen} stays nearly constant due to the balance between the dUrca heat loss and the heat income through the interface with the hotter outer core. During this stage, the outer-core temperature T_{out} decreases due to the neutrino emission and the leakage of heat into the dUrca kernel, while the heat flux through the outer boundary of the core is much smaller than the neutrino luminosity and does not affect the heat evolution. Here, for simplicity, we retain only the leading heat loss mechanism in the outer core. Accordingly, this cooling stage is further divided in two substages. As long as T_{out} is sufficiently high, the cooling of the outer core is controlled by the mUrca processes (Section 5.3). As soon as T_{out} has decreased so that the mUrca power is smaller than the flux through the inner boundary, the *core thermalization* substage begins, which is controlled by heat transport (Section 5.4). This separation into two substages is eliminated in Appendix A, where both the mUrca and conductive cooling of the outer core are jointly taken into account.

The third stage begins when T_{cen} and T_{out} become nearly equal. It is the familiar neutrino cooling stage of an isothermal core (Section 5.5).

Eventually the core temperature falls so low that the neutrino luminosity is smaller than heat flux through the outer core boundary. This manifests the transition to the photon cooling stage, which is not considered in the present work.

For a qualitative comparing our toy model results with observations, we need a relation between the effective surface temperature T_s of the star (at $r = R$) and the temperature T_{cc} at the crust-core interface ($r = R_{core}$). We note that for the cooling models studied in this paper at $T_{cc} \lesssim 5 \times 10^8$ K, one can use a simple power-law relation

$$T_s = T_{s0}\, T_{cc8}^{\beta_{cc}}, \quad (13)$$

where $\beta_{cc} \approx 0.55$, $T_{cc8} = T_{cc}/10^8$ K, and T_{s0} is a normalization constant dependent on a specific NS model. The validity of this relation is demonstrated in Fig. 12, where four thicker lines of different types and colors are taken from the results of exact numerical simulations demonstrated in Fig. 7. The four related dotted lines display our approximation, Eq. (13), with appropriate values of T_{s0}. The approximation seems reasonably accurate. It allows us to estimate an important observable,

the slope of $L_\gamma(t)$ cooling curve,

$$s_L = \frac{\mathrm{d}\log L_\gamma}{\mathrm{d}\log t} \approx 4\beta_{\rm cc}\frac{\mathrm{d}\log T_{\rm cc}}{\mathrm{d}\log t}, \quad (14)$$

introduced in Section 2.

5.2. Local cooling stage: formation of cold kernel

This initial local cooling stage lasts till the onset of a quasi-stationary thermal equilibrium in the dUrca kernel (as discussed below). At the local stage, any elementary volume element loses heat mostly via neutrino emission, while thermal conduction is inefficient. The cooling equation reduces to

$$c_V\frac{\mathrm{d}T}{\mathrm{d}t} = -Q, \quad (15)$$

where $T = T_{\rm cen}$ and $Q = Q_{\rm D}$ in the dUrca kernel, while $T = T_{\rm out}$ and $Q = Q_{\rm M}$ in the outer core. Then we easily obtain the time, required to cool the dUrca kernel to a temperature $T_{\rm cen}$,

$$t = \frac{c_0}{4Q_{\rm D0}}\left(\frac{1}{T_{\rm cen}^4} - \frac{1}{T_{\rm init}^4}\right), \quad (16)$$

where $T_{\rm init}$ is the initial temperature. Assuming $T_{\rm init} \gg T_{\rm cen}$, we have

$$T_{\rm cen} \approx \left(\frac{c_0}{4Q_{\rm D0}\,t}\right)^{1/4}. \quad (17)$$

Analogously, the temperature $T_{\rm out}$ in the outer core decreases as

$$T_{\rm out} \approx \left(\frac{c_0}{6Q_{\rm M0}\,t}\right)^{1/6}. \quad (18)$$

With our parameter values in Eqs. (9)–(11), we can easily check that, initially, $T_{\rm out} \gg T_{\rm cen}$. Then the kernel stays much colder than the outer core (Fig. 10), and the neutrino luminosity of the star is mostly determined by mUrca processes in the outer core (Fig. 8),

$$L_{\rm M} \approx Q_{\rm M0}T_{\rm out}^8 V_{\rm out} \approx 0.56\times10^{33} g_{\rm M} R_{11}^3 T_{\rm o8}^8 \ \mathrm{erg\ s^{-1}}. \quad (19)$$

Here $T_{\rm o8} = T_{\rm out}/10^8$ K, $V_{\rm out} = V_{\rm core} - V_{\rm D}$ is the outer core volume, $V_{\rm core} = (4\pi/3)R_{\rm core}^3$, $V_{\rm D} = (4\pi/3)r_{\rm D}^3$, $R_{\rm core}$ is the core radius, and $R_{11} \equiv R_{\rm core}/(11\ \mathrm{km})$. Taking into account that $r_{\rm D}^3 \ll R_{\rm core}^3$, this means that early NS cooling is almost unaffected by the dUrca kernel.

The local cooling stage does not last very long, but similar conclusions remain true at the first phase of the second cooling stage for the outer core (see below).

The regime of free neutrino cooling of the dUrca kernel, described by Eq. (17), is violated once the thermal conduction time $t_{\rm tr,D}$ through the kernel becomes comparable with current time t. The conduction time can be evaluated as (cf. Henyey and L'Ecuyer, 1969)

$$t_{\rm tr,D}(T_{\rm cen}) \approx \frac{c_V}{\varkappa}\frac{r_{\rm D}^2}{4} = \frac{c_0}{4\varkappa_0}T_{\rm cen}^2 r_{\rm D}^2 \approx 0.024\frac{g_c}{g_\varkappa}r_{\rm D1}^2 T_{\rm c8}^2\ \mathrm{yr}, \quad (20)$$

where $T_{\rm c8} = T_{\rm cen}/(10^8\ \mathrm{K})$. By substituting $t_{\rm tr,D}$ into Eq. (16) we estimate the quasi-stationary temperature established in the center of the star by the end of the local cooling[2]

$$T_{\rm qst} \approx \left(\frac{\varkappa_0}{Q_{\rm D0}\,r_{\rm D}^2}\right)^{1/6} \approx 10^8\left(\frac{g_\varkappa}{g_{\rm D}}\right)^{1/6} r_{\rm D1}^{-1/3}\ \mathrm{K}, \quad (21)$$

so that the duration of this stage is

$$t_{\rm loc} \approx t_{\rm tr,D}(T_{\rm qst}) = \frac{c_0}{4}\left(\frac{r_{\rm D}^4}{\varkappa_0^2 Q_{\rm D0}}\right)^{1/3} \approx 0.024\frac{g_c}{g_\varkappa^{2/3}g_{\rm D}^{1/3}}r_{\rm D1}^{4/3}\ \mathrm{yr}, \quad (22)$$

in a qualitative agreement with exact calculations (Fig. 10).

5.3. Stage with cold kernel: cooling via mUrca neutrinos

In the beginning of NS cooling with the cold dUrca kernel, the temperature in the outer core is mostly regulated by mUrca processes. The radial temperature profile in the outer core stays rather smooth (Fig. 10). In contrast, the temperature in the kernel and nearby outer layers remains a sharp function of r; the stellar center is the coldest place in the core. Because of strong thermal coupling of the kernel with the outer core after the onset of this stage, the radial temperature profile in the kernel becomes quasi-stationary and varies slowly in time (cf. Sales et al., 2020). This quasi-stationarity implies thermal balancing of the kernel,

$$4\pi r_{\rm D}^2 F_{\rm D} \approx L_{\rm D}, \quad (23)$$

where $F_{\rm D} = -\kappa\,\partial T/\partial r|_{r=r_{\rm D}}$ is the density of radial heat flux conduced from the outer core to the kernel (at $r = r_{\rm D}$), and

$$L_{\rm D} = \frac{4\pi}{3}\int_0^{r_{\rm D}} Q_{\rm D}(r)\,r^2\,\mathrm{d}r \approx V_{\rm D}\,Q_{\rm D0}T_{\rm cen}^6 \quad (24)$$

is the neutrino luminosity of the kernel.

Eq. (19) for the outer core and the last approximate equality in Eq. (24) are based on our approximation of steplike temperature profile. More accurate quasi-stationary temperature profiles within the kernel and around it can be calculated at any moment of time by solving the stationary heat-balance equations

$$-\nabla\cdot\boldsymbol{F} = Q, \quad \boldsymbol{F} = -\varkappa\nabla T, \quad (25)$$

where $\boldsymbol{F}$ is the heat flux density. In our case, it is sufficient to solve an ordinary one-dimensional heat diffusion equation with neutrino energy sinks. This procedure can be easily generalized to arbitrary dependence of κ and Q on density and temperature. Also, it allows one to properly include the effects of nucleon superfluidity and General Relativity, building thus a reasonably accurate model of quasi-stationary NS cooling. However, it is out the scope of this paper.

As seen from numerical simulations (Sales et al. 2020 and our Fig. 10), temperature profiles are flat inside the kernel with

[2] Comparing our analytical estimates with numerical results, one should remember that the redshift factor, which is neglected here, reaches ~ 0.4–0.6 at the center of NS models shown in Fig. 10.

a sharp jump at $r = r_{\rm D}$ at the local cooling stage, but become smoother at $t \gtrsim t_{\rm loc}$, as thermal conduction comes into play. When cooling goes on, $T_{\rm cen}$ decreases much slower than $T_{\rm out}$.

At the mUrca cooling stage, Eq. (17) becomes invalid and should be replaced by the condition of quasi-stationary thermal coupling of the kernel, Eq. (23). Because $T_{\rm cen}$ decreases with time very slowly, it would be a reasonable approximation to use constant $T_{\rm cen}$ given by Eq. (21). Then

$$T_{\rm cen} \approx T_{\rm qst}, \quad L_{\rm D} \approx \frac{4\pi}{3}\varkappa_0 r_{\rm D} \approx 4\times 10^{36} g_\varkappa r_{\rm D1}\ {\rm erg\ s^{-1}}. \quad (26)$$

As already noted, at this stage the star cools mainly via neutrino emission from the outer core; the total heat conduction flux and subsequent neutrino emission from the dUrca kernel are weak. The heat flux through the outer boundary of the core ($r = R_{\rm core}$) is meant to be negligibly small. Accordingly, we can describe the mUrca cooling of the core at $r > r_{\rm D}$ by the equation

$$c_V V_{\rm out}\frac{{\rm d}T_{\rm out}}{{\rm d}t} = -L_{\rm M}. \quad (27)$$

Eqs. (19) and (27) yield the same Eq. (18) as at the local cooling stage.

Strictly speaking, at the beginning of NS cooling with cold kernel the outer core remains thermally non-coupled by itself. The characteristic coupling time $t_{\rm tr,M}$ can be estimated in the same manner as $t_{\rm tr,D}$:

$$t_{\rm tr,M}(T_{\rm out}) \approx \frac{c_V}{\varkappa}\frac{R_{\rm out}^2}{4} \approx 2.4\frac{g_c}{g_\varkappa}R_{\rm o10}^2 T_{\rm o8}^2\ {\rm yr}, \quad (28)$$

where $R_{\rm out} = R_{\rm core} - r_{\rm D}$ is the outer-core thickness and $R_{\rm o10} \equiv R_{\rm out}/(10\ {\rm km})$. Accordingly, the thermal coupling of the entire core occurs at the age

$$t_{\rm M0} \approx \frac{c_0}{4}\left(\frac{2R_{\rm out}^6}{3\varkappa_0^3 Q_{\rm M0}}\right)^{1/4} \approx 38\frac{g_c}{g_\varkappa^{3/4} g_{\rm M}^{1/4}}R_{\rm o10}^{3/2}\ {\rm yr}. \quad (29)$$

Nevertheless, thermal couplings in the outer core and in the dUrca kernel are different. The coupling within the outer core should produce thermal equilibration (isotropic temperature distribution) due to high thermal conductivity. But the temperature is already isotropic in the outer core, by construction of the toy model. Further neutrino mUrca cooling (18) does not violate this isothermality. Thermal coupling in the dUrca kernel is of different nature, being accompanied by a steady heat sinking into the core in the presence of a large quasi-stationary temperature drop.

In accurate numerical simulations (Fig. 10), one obtains slightly non-isothermal outer cores, with persistent quasi-stationary thermal fluxes sinking into the dUrca kernel from the entire outer core. This effect is stronger in more massive NSs: compare the upper and lower panels in Fig. 10. At large times (Section 5.5) the kernel will fully equilibrate with the outer core, making the entire core isothermal. The temperature drops at $r > R_{\rm core}$ in Fig. 10 are associated with heat fluxes directed to the stellar surface and neglected in the toy model.

In the toy model, the temperature at the crust-core interface $T_{\rm cc} = T_{\rm out}$. Then the cooling curve slope (14) during the mUrca cooling stage is $s_L = (2/3)\beta_{\rm cc} \approx 0.4$. The actual slope is noticeably larger, because $T_{\rm out}$ is a proper estimate of the mean temperature of the outer core. The toy-model $T_{\rm out}$ can differ from numerically calculated $T_{\rm cc}$ because of some thermal heat flux to the NS kernel and some heat outflow from the core to the surface.

The cooling phase we study in this subsection lasts as long as $L_{\rm M} \gtrsim L_{\rm D}$. The condition $L_{\rm M} \approx L_{\rm D}$ gives the outer core temperature at the end of this phase,

$$T_{\rm MD} \approx \left(\frac{r_{\rm D}^3\, Q_{\rm D0} T_{\rm qst}^6}{R_{\rm core}^3\, Q_{\rm M0}}\right)^{1/8} = \left(\frac{r_{\rm D}\varkappa_0}{R_{\rm core}^3 Q_{\rm M0}}\right)^{1/8} \approx \frac{3\times 10^8}{R_{11}^{3/8}}\frac{g_\varkappa^{1/8} r_{\rm D1}^{1/8}}{g_{\rm M}^{1/8}}\ {\rm K}. \quad (30)$$

Substitution of $T_{\rm out} = T_{\rm MD}$ into Eq. (18) gives the corresponding age

$$t_{\rm MD} \approx \frac{c_0 R_{\rm core}^{9/4}}{6 Q_{\rm M0}^{1/4}\varkappa_0^{3/4} r_{\rm D}^{3/4}} \approx 200\frac{R_{11}^{9/4} g_c}{g_{\rm M}^{1/4} g_\varkappa^{3/4}} r_{\rm D1}^{-3/4}\ {\rm yr}. \quad (31)$$

5.4. Stage with cold kernel: thermalization

At $t \gtrsim t_{\rm MD}$ the outer core starts to cool predominantly via heat transport into the dUrca kernel and neutrino emission from it. For some time the dUrca kernel still stays colder than the mUrca core, as in Section 5.3.

In the toy model, we keep Eq. (19) for $L_{\rm M}$ and Eqs. (23), (24) for $L_{\rm D}$. Now the cooling equation reads

$$c_V V_{\rm out}\frac{{\rm d}T_{\rm out}}{{\rm d}t} \approx -4\pi r_{\rm D}^2 F_{\rm D} \approx -L_{\rm D}. \quad (32)$$

Using Eq. (26), we arrive at

$$\frac{{\rm d}T_{\rm out}}{{\rm d}t} \approx -\frac{Q_{\rm D0} T_{\rm cen}^6 \delta_V}{c_0 T_{\rm out}}, \quad (33)$$

where $\delta_V = V_{\rm D}/V_{\rm out} = r_{\rm D}^3/(R_{\rm core}^3 - r_{\rm D}^3)$ is the volume ratio of the dUrca kernel and the rest of the core.

The most sensitive problem is to estimate $T_{\rm cen}$. In contrast to the mUrca cooling stage, where $T_{\rm cen}$ was safely approximated as constant $T_{\rm qst}$, at this stage $T_{\rm cen}$ is more variable. Nevertheless, we will keep $T_{\rm cen} = T_{\rm qst}$, for simplicity.

Then Eq. (33) has the solution

$$T_{\rm out}^2 \approx T_{\rm MD}^2 - \frac{2Q_{\rm D0} T_{\rm qst}^6 \delta_V}{c_0}(t - t_{\rm MD}), \quad (34)$$

which approximately describes cooling and temperature equilibration between the kernel and outside core. The duration of this equilibration $\Delta t_{\rm eq} = t_{\rm eq} - t_{\rm MD}$ can be estimated by equating $T_{\rm out} = T_{\rm qst}$ in Eq. (34), which gives

$$\Delta t_{\rm eq} \approx \frac{1}{2}\left(\frac{T_{\rm MD}^2}{T_{\rm qst}^2} - 1\right)\frac{c_0}{Q_{\rm D0}\delta_V T_{\rm qst}^4}, \quad (35)$$

about three centuries for our typical toy model parameters. Thus $t_{\rm eq} \equiv t_{\rm MD} + \Delta t_{\rm eq} \sim 500$ yr.

5.5. DUrca cooling stage with nearly isothermal core

At $t \gtrsim t_{\rm eq}$ the temperatures $T_{\rm cen}$ and $T_{\rm out}$ become nearly equal. It is the familiar neutrino cooling stage of an isothermal core, in which case the cooling equation reduces to

$$c_V V_{\rm core} \frac{{\rm d}T}{{\rm d}t} = -L_{\rm D}. \tag{36}$$

Then

$$\frac{{\rm d}T}{{\rm d}t} = -\frac{V_{\rm D}}{V_{\rm core}} \frac{Q_{\rm D}}{c_V} \approx -\left(\frac{r_{\rm D}}{R_{\rm core}}\right)^3 \frac{Q_{\rm D0}}{c_0} T^5. \tag{37}$$

In our toy model, $T = T_{\rm qst}$ at $t = t_{\rm eq} = t_{\rm MD} + \Delta t_{\rm eq}$, which gives the solution

$$\frac{1}{T^4} = \frac{1}{T_{\rm qst}^4} + \left(\frac{r_{\rm D}}{R_{\rm core}}\right)^3 \frac{4Q_{\rm D0}}{c_0} (t - t_{\rm eq}). \tag{38}$$

At $t \gtrsim t_{\rm eq}$ this equation with the use of Eq. (13) and Eq. (14) ($T_{\rm cc} = T$) gives us the slope of the cooling curve

$$s_L = \left(\frac{r_{\rm D}}{R_{\rm core}}\right)^3 \frac{4Q_{\rm D0}}{c_0} \beta_{\rm cc}\, t\, T^4. \tag{39}$$

Accordingly, s_L changes from its maximum value at $t = t_{\rm eq}$,

$$s_L(t_{\rm eq}) \sim 10\beta_{\rm cc} \frac{g_{\rm D}}{g_c} \frac{r_{\rm D1}^3}{R_{11}^3} \left(\frac{T_{\rm qst}}{10^8\ {\rm K}}\right)^4 \frac{t_{\rm eq}}{300\ {\rm yr}}, \tag{40}$$

to $s_L \approx \beta_{\rm cc}$ at $t \gg t_{\rm eq}$.

Clearly, the toy-model estimates cannot pretend to be very accurate.

6. Conclusions

We have studied a remarkable phenomenon of rapidly cooling Cas A NS observed in real time. We have summarized current status of the Cas A NS observations and compared possible interpretations of the data in terms of surface temperature or photon luminosity.

We have presented numerical simulations of Cas A NS cooling in frames of several theoretical scenarios, confronted the results with observations and analysed respective constraints on microphysical theories of NS matter. We have focused on the well known PBF and hybrid scenarios and proposed the new Urca scenario. The latter is based on the 'delayed rapid cooling' phenomenon, previously studied by Sales et al. (2020). It occurs in NSs with small central dUrca kernels, where the neutrino emission is enhanced by dUrca processes. Such kernels stay at a nearly constant temperature for a long time till their thermal equilibration with the outer core, which delays the onset of rapid cooling via dUrca neutrino emission.

We have demonstrated that this mechanism can naturally explain the observed rapid cooling of the Cas A NS, regardless of superfluidity and the PBF cooling mechanism. It shares some features with the hybrid cooling scenario (Leinson, 2022; Tu and Li, 2025), in which the dUrca cooling assists the PBF mechanism. Unlike the PBF and hybrid scenarios, the Urca scenario does not require the NS core temperature to be slightly lower than the critical temperature $T_{\rm nt}$ in the present epoch. We have shown that the observed cooling rate can be explained without special assumptions about baryon superfluidity or efficiency of the PBF energy losses. This reconciles the observed rate with modern theoretical results which predict weak efficiency of the PBF mechanism (Leinson, 2010) and a narrow density range allowed for proton superfluidity (e.g., Baldo and Schulze, 2007; Guo et al., 2019; Lim and Holt, 2021). The suppression of proton superfluidity shifts the onset of PBF processes to earlier times, incompatible with the Cas A NS age, making such processes irrelevant for explaining the observed Cas A NS cooling, regardless of their efficiency.

The main problem of the proposed Urca scenario for the Cas A NS cooling consists in the inevitable NS mass tuning, which is required to get the dUrca kernel radius $r_{\rm D} \sim 0.7$–1.5 km. On the other hand, as we show in Section 4.1, the popular PBF cooling scenario also requires a serious tuning of model input parameters in order to simultaneously match the absolute value and decline rate of the photon luminosity $\widetilde{L}_\gamma$ at the current Cas A NS age. All other attempts to explain the Cas A NS phenomena (Section 1) suffer from the problem of fine tuning of model parameters as well.

For any NS with $M > M_{\rm DU}$, the enhanced cooling stage exists, regardless of superfluidity model, for any NS with a dUrca kernel; the value of $r_{\rm D}$ affects only the age at which this enhanced cooling starts to operate. This is additionally clarified by our analytic toy model (Section 5 and Appendix A). It demonstrates self-similarity and parametric dependencies of cooling curves in the Urca scenario. Our analytical scaling relations agree with the numerical results presented in Section 4, as well as with those obtained by Sales et al. (2020).

Another notice is that the hybrid and Urca scenarios require the cooling stage with cold dUrca kernel, while the PBF scenario not (e.g., Shternin and Yakovlev 2015).

Funding

This research is supported by the Russian Science Foundation Grant No. 24-12-00320.

CRediT authorship contribution statement

A.Y. Potekhin: Conceptualization, Methodology, Software, Formal analysis, Investigation, Visualization, Writing – original draft, Writing – review & editing. **D.G.Yakovlev:** Formal analysis, Writing – review & editing.

Declaration of competing interest

The authors declare that they have no known competing financial interests or personal relationships that could have appeared to influence the work reported in this paper.

Data availability

The data pertinent to this research will be made available on a request to the corresponding author.

Appendix A. Cooling of the outer core

In equations for cooling of the outer core via mUrca neutrinos in Section 5.3 we neglected the heat flux $4\pi r_{\rm D}^2 F_{\rm D} \approx L_{\rm D}$ from the outer core into the dUrca kernel. Vice versa, in Eq. (32) we included the heat flux but neglected $L_{\rm M}$. Now we include both processes together. Then the cooling equation for the outer core ($r_{\rm D} < r < R_{\rm core}$) over the entire stage of cold kernel reads

$$c_V V_{\rm out} \frac{{\rm d}T_{\rm out}}{{\rm d}t} = -L_{\rm M} - 4\pi r_{\rm D}^2 F_{\rm D}. \qquad (A.1)$$

The first term on the right-hand-side is the neutrino luminosity of the outer core, and the second term is the rate of thermal energy losses due to heat conduction into the dUrca kernel. Since the heat inflow into the kernel is nearly balanced by the neutrino emission from there, we replace $4\pi r_{\rm D}^2 F_{\rm D}$ by $L_{\rm D}$ according to Eq. (23). Dividing both sides of Eq. (A.1) by the outer-core volume $V_{\rm out}$, we obtain

$$c_0 T_{\rm out} \frac{{\rm d}T_{\rm out}}{{\rm d}t} = -Q_{\rm M0} T_{\rm out}^8 - \delta_V \bar{Q}_{\rm D}, \qquad (A.2)$$

where $\bar{Q}_{\rm D} = 3F_{\rm D}/r_{\rm D} \approx L_{\rm D}/V_{\rm D} \approx Q_{\rm D0} T_{\rm cen}^6$. We will treat $T_{\rm cen}$ as constant, because it decreases much slower than $T_{\rm out}$ as long as the outer core stays hotter than the kernel (see Sections 4.3 and 5).

Substitutions

$$z = \left(\frac{Q_{\rm M0}}{\delta_V \bar{Q}_{\rm D}}\right)^{1/4} T_{\rm out}^2, \quad x = \frac{2\delta_V \bar{Q}_{\rm D}}{c_0} \left(\frac{Q_{\rm M0}}{\delta_V \bar{Q}_{\rm D}}\right)^{1/4} t \qquad (A.3)$$

reduce Eq. (A.2) to

$$\frac{{\rm d}z}{{\rm d}x} = -(z^4 + 1). \qquad (A.4)$$

The latter equation has analytic solution (e.g., Gradshteyn and Ryzhik 2015)

$$x = \frac{1}{2\sqrt{2}} \arctan \frac{z\sqrt{2}}{z^2 - 1} - \frac{1}{4\sqrt{2}} \ln \frac{1 + z\sqrt{2} + z^2}{1 - z\sqrt{2} + z^2} + x_0, \qquad (A.5)$$

where x_0 is a constant. At $z > 1$ we take $x_0 = 0$. With this choice we satisfy the initial condition $z \to \infty$ at $x \to 0$ and reproduce the law of purely mUrca cooling, Eq. (18), at early ages. At $z < 1$ we take $x_0 = \pi/2^{3/2}$ which ensures the continuity of the solution across the point $z = 1$, provided that the principal value of arctangent is assumed.

Such a solution allows us to avoid splitting the cooling stage with quasi-stationary NS kernel in two parts, where the cooling is regulated either by mUrca (Section 5.3) or by dUrca (Section 5.4) neutrinos. The solution does not contain the characteristic age $t_{\rm MD}$ at which the mUrca and dUrca neutrino luminosities become comparable, but contains a single characteristic age $t_{\rm eq}$ of thermal equilibration of the dUrca kernel with the outer core. We can find $t_{\rm eq}$ from Eqs. (A.3) and (A.5) by substituting $T_{\rm out} = T_{\rm qst}$. Then Eqs. (A.3) and (A.5) describe the cooling at $t < t_{\rm eq}$ (skipping the short local cooling stage, Section 5.2). As previously, the late dUrca cooling stage at $t > t_{\rm eq}$ (Section 5.5) is described by Eq. (38). The value of $t_{\rm eq}$ obtained in this way provides a correction to the estimate of $t_{\rm eq}$, obtained in Section 5.4 for a cruder model. Of course, in reality the core equilibration proceeds smoothly together with the subsequent cooling, so that 'exact definition' of $t_{\rm eq}$ is not so important.

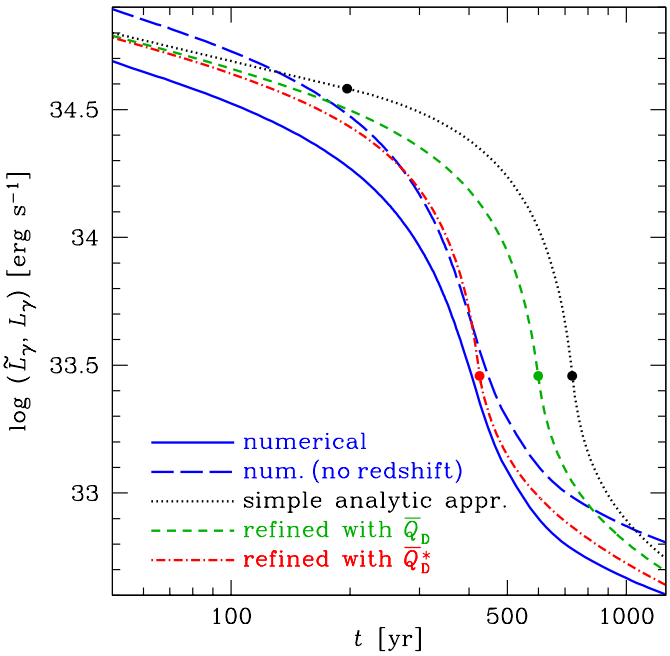

Figure A.1: Analytical approximations for the Urca cooling curves compared with simulations. The blue solid curve is the same as in Fig. 9. The blue long-dashed curve is the same but neglecting gravitational redshift correction. Other three lines are analytical approximations with the NS parameters consistent with those for the blue curves: $R = 12.7$ km, $R_{\rm core} = 11.7$ km, $r_{\rm D} = 1.2$ km; Eq. (13) is applied with $T_{\rm s0} = 1.3$ MK that is suitable for carbon heat-blanketing envelope. The black dotted line is plotted according to simplified analytical formulas of Section 5. The green short-dashed curve is the approximation given in Appendix A. The red dot-dashed curve is the same as the red dot-dashed one but assuming a correction factor $g_{\rm D} = 1.6$ in Eq. (9). Heavy dots mark matching points between different segments of analytic solutions.

The resulting approximation is illustrated by the short-dashed line in Fig. A.1. For comparison, the dotted line shows more simplified approximation from Section 5, and the solid line reproduces numerical simulations from Fig. 9. In Fig. A.1, we use analytic approximations with the parameters $R_{\rm core} = 11.7$ km and $r_{\rm D} = 1.2$ km, which are the same as in Figs. 9 and 10. The temperature in the outer core is converted into L_γ using Eq. (2) at $R = 12.7$ km with $T_{\rm s0} = 1.3$ MK, also in agreement with the numerical model. All correction factors are assumed to be $g_{\rm M} = g_{\rm D} = g_c = g_\varkappa = 1$. To demonstrate typical effects of General Relativity corrections, neglected in our analytic approximations, the long-dashed curve in Fig. A.1 displays the photon luminosity simulated neglecting redshift corrections. Heavy dots separate different cooling regimes (Section 5) on analytic curves. Since the curves are smooth, this gives another confirmation that separating different cool-

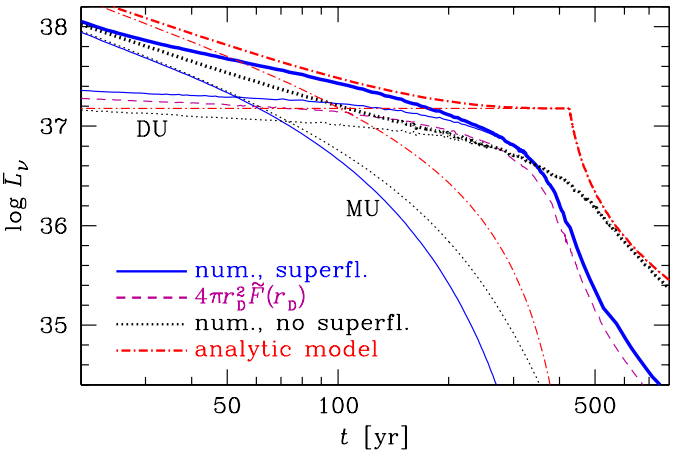

Figure A.2: Comparison of numerical solutions and analytical approximations of neutrino luminosities in the Urca cooling scenario. Thick solid and dotted lines show numerically calculated total redshifted neutrino luminosities for the NS models with and without nucleon superfluidity, whose cooling curves are presented in Fig. 9. The dot-dashed red line is the total neutrino luminosity in the analytical model; it corresponds to the cooling curve of the same type in Fig. A.1. Thin lines of the same types are partial luminosities due to mUrca (marked MU) and dUrca (DU) processes. The thin dashed line is the heat flux from the outer core to the dUrca kernel, numerically calculated for the superfluid NS model.

ing regimes by specific points is, indeed, very conditional. As mentioned above, our approximation of a constant temperature $T = T_{\rm cen}$ in the dUrca kernel is rather crude. The real temperature smoothly increases from the center to the boundary of the dUrca kernel. Therefore, the mean value of $Q_{\rm D}$ is higher than $Q_{\rm D0} T_{\rm cen}^6$. In addition, as we noted in Section 5.1, the employed values of model parameters are only approximations up to factors of a few. To show the importance of these effects, the red dot-dashed curve in Fig. 9 is obtained with the value of $Q_{\rm D}$ increased by setting $g_{\rm D} = 1.6$ in Eq. (9).

Fig. A.2 shows the total and partial (mUrca and dUrca) numerical neutrino luminosities in superfluid and non-superfluid NS models and the same luminosities in the analytic approximation developed in this appendix, as functions of time. An additional line shows the heat flux through the surface of the dUrca kernel in a superfluid NS. Its proximity to the dUrca luminosity at all times confirms the validity of Eq. (23). Comparing Fig. A.2 with Fig. A.1, we are convinced once more that observable surface photon luminosities are rather insensitive to details of respective neutrino luminosities.

The presented approach can be further improved, first of all by calculating exact temperature profiles in the dUrca kernel and nearby outside layers using the quasi-stationary approximation, as discussed in Sec. 5.4. This would allow one to find more reliable values of $T_{\rm qst}$ and follow their evolution along cooling tracks, instead of relying on a simplified estimate of constant $T_{\rm qst}$, Eq. (21). Also, it may help modeling realistic temperature gradients in the outer core in the presence of cold dUrca kernel. Another weak point of the approach presented in this appendix is that (by construction) it guarantees continuity of $T(t)$, $L_\nu(t)$, and $\mathrm{d}T/\mathrm{d}t$ at the matching point $t = t_{\rm eq}$, but does not guarantee continuity of $\mathrm{d}L_\nu/\mathrm{d}t$. As a result, we obtain an unrealistic kink of $L_\nu(t)$ at $t = t_{\rm eq}$ on the dot-dashed curve in Fig. A.2. Such kinks can also be eliminated in frames of accurate quasi-stationary calculations. However, such a refined model would hardly allow a simple analytical solution, like the one presented here.

References

Akmal A., Pandharipande V.R., Ravenhall D.G., 1998. Equation of state of nucleon matter and neutron star structure, Phys. Rev. C, 58, 1804.

Alford J.A.J., Halpern J.P., 2023. Do central compact objects have carbon atmospheres? Astrophys. J., 944, 36.

Amundsen, L., Østgaard, E., 1985. Superfluidity of neutron matter (II). Triplet pairing. Nucl. Phys. A, 442, 163.

Avila, A., Giangrandi, E., Sagun, V., Ivanitskyi, O., Providência, C., 2024. Rapid neutron star cooling triggered by dark matter, Mon. Not. R. Astron. Soc., 528, 6319.

Ashworth, W.B., 1980. A probable Flamsteed observation of the Cassiopeia A supernova. J. Hist. Astron., 11, 1.

Baldo, M., Schulze, H.-J., 2007. Proton pairing in neutron stars. Phys. Rev. C, 75, 025802.

Baldo, M., Elgarøy, Ø., Engvik, L., Hjorth-Jensen, M., Schulze, H.J., 1998. $^3P_2$–$^3F_2$ pairing in neutron matter with modern nucleon-nucleon potentials. Phys. Rev. C, 58, 1921.

Bardeen, J., Cooper, L.N., and Schrieffer, J.R., 1957. Theory of superconductivity. Phys. Rev., 108, 1175.

Blaschke, D., Grigorian, H., Voskresensky, D.N., Weber F., 2012. Cooling of the neutron star in Cassiopeia A. Phys. Rev. C, 85, 022802.

Blaschke, D., Grigorian, H., Voskresensky, D.N., 2013. Nuclear medium cooling scenario in light of new Cas A cooling data and the $2M_\odot$ pulsar mass measurements. Phys. Rev. C, 88, 065805

Bonanno, A., Baldo, M., Burgio, G.F., Urpin, V., 2014. The neutron star in Cassiopeia A: equation of state, superfluidity, and Joule heating. Astron. Astrophys., 561, L5.

Chen, J.M.C., Clark, J.W., Davé, R.D., Khodel, V.V., 1993. Pairing gaps in nucleonic superfluids. Nucl. Phys. A, 555, 59.

Ding, D., Rios, A., Dussan, H., Dickhoff, W.H., Witte, S.J., Carbone, A., Polls, A., 2016. Pairing in high-density neutron matter including short- and long-range correlations. Phys. Rev. C, 94, 025802.

Elgarøy, Ø., Engvik, L., Hjorth-Jensen, M., Osnes, E., 1996a. Triplet pairing of neutrons in β-stable neutron star matter. Nucl. Phys. A, 607, 425.

Elgarøy, Ø., Engvik, L., Hjorth-Jensen, M., Osnes, E., 1996b. Superfluidity in β-stable neutron star matter. Phys. Rev. Lett., 77, 1428.

Elshamouty, K.G., Heinke, C.O., Sivakoff, G.R., Ho, W.C.G., Shternin, P.S., Yakovlev, D.G., Patnaude, D.J., David, L., 2013. Measuring the cooling of the neutron star in Cassiopeia A with all Chandra X-ray observatory detectors. Astrophys. J., 777, 22.

Fesen R.A., Hammell, M.C., Morse, J., Chevalier, R.A., Borkowski, K.J., Dopita, M.A., Gerardy, C.L., Lawrence, S.S., Raymond, J.C., van den Bergh, S., 2006. The expansion asymmetry and age of the Cassiopeia A supernova remnant. Astrophys. J., 645, 283

Flowers, E., Ruderman, M., Sutherland, P., 1976. Neutrino pair emission from finite-temperature neutron superfluid and the cooling of young neutron stars. Astrophys. J., 205, 541.

Gandolfi, S., Illarionov, A.Yu., Pederiva, F., Schmidt, K.E., Fantoni S., 2009. Equation of state of low-density neutron matter, and the $^1S_0$ pairing gap. Phys. Rev. C, 80, 045802.

Gandolfi, S., Palkanoglou, G., Carlson, J., Gezerlis, A., Schmidt, K.E., 2022. The $^1S_0$ pairing gap in neutron matter. Condens. Matter, 7, 19.

Glen, G., Sutherland, P., 1980. On the cooling of neutron stars. Astrophys. J., 239, 671.

Gnedin, O.Y., Yakovlev, D.G., Potekhin, A.Y., 2001. Thermal relaxation in young neutron stars. Mon. Not. R. Astron. Soc., 324, 725.

Goriely, S., Chamel, N., Pearson, J.M., 2013. Further explorations of Skyrme-Hartree-Fock-Bogoliubov mass formulas. XIII. The 2012 atomic mass evaluation and the symmetry coefficient. Phys. Rev. C, 88, 024308.

Gradshteyn, I.S., Ryzhik, I.M., 2015. Table of Integrals, Series, and Products, 8th ed. Elsevier, Amsterdam.

Guo, W., Dong, J.M., Shang, X., Zhang, H.F., Zuo, W., Colonna, M., Lombardo, U., 2019. Proton-proton $^1S_0$ pairing in neutron stars. Nucl. Phys. A, 986, 18.

Hamaguchi, K., Nagata, N., Yanagi, K., Zheng, J., 2018. Limit on the axion decay constant from the cooling neutron star in Cassiopeia A. Phys. Rev. D, 98, 103015.

Heinke C.O., Ho W.C.G., 2010. Direct observation of the cooling of the Cassiopeia A neutron star. Astrophys. J., 719, L167.

Henyey, L., L'Ecuyer, J.L., 1969. Studies in stellar evolution. VIII. The time scale for the diffusion of energy in the stellar interior. Astrophys. J., 156, 549.

Ho W.C.G., Heinke C.O., 2009. A neutron star with a carbon atmosphere in the Cassiopeia A supernova remnant. Nature, 462, 71.

Ho W.C.G., Elshamouty K.G., Heinke C.O., Potekhin A.Y., 2015. Tests of the nuclear equation of state and superfluid and superconducting gaps using the Cassiopeia A neutron star. Phys. Rev. C, 91, 015806.

Ho W.C.G., Zhao, Y., Heinke, C.O., Kaplan, D.L., Shternin, P.S., Wijngaarden, M.J.P., 2021. X-ray bounds on cooling, composition, and magnetic field of the Cassiopeia A neutron star and young central compact objects. Mon. Not. R. Astron. Soc., 506, 5015.

Horowitz, C.J., Piekarewicz, J., Reed B., 2020. Insights into nuclear saturation density from parity-violating electron scattering. Phys. Rev. C, 102, 044321.

Kaminker, A.D., Haensel, P., Yakovlev, D.G., 2001. Nucleon superfluidity vs. observations of cooling neutron stars. Astron. Astrophys., 373, L17.

Kantor, E.M., Gusakov, M.E., 2009. The neutrino emission due to plasmon decay and neutrino luminosity of white dwarfs. Mon. Not. R. Astron. Soc., 381, 1702.

Kolomeitsev, E.E., Voskresensky, D.N., 2008. Neutrino emission due to Cooper-pair recombination in neutron stars reexamined. Phys. Rev. C, 77, 065808.

Kolomeitsev, E.E., Voskresensky, D.N., 2010. Neutral weak currents in nucleon superfluid Fermi liquids: Larkin-Migdal and Leggett approaches. Phys. Rev. C, 81, 065801.

Krotschek, E., Papakonstantinou, P., Wang, J., 2023. Triplet pairing in neutron matter. Astrophys. J., 955, 76.

Krotschek, E., Papakonstantinou, P., Wang, J., 2024. Variational and parquet-diagram calculations for neutron matter. V. Triplet pairing. Phys. Rev. C, 109, 015803.

Leinson, L.B., 2009. Superfluid response and the neutrino emissivity of baryon matter: Fermi-liquid effects. Phys. Rev. C, 79, 045502.

Leinson, L.B., 2010. Neutrino emission from triplet pairing of neutrons in neutron stars. Phys. Rev. C, 81, 025501.

Leinson, L.B., 2014. Axion mass limit from observations of the neutron star in Cassiopeia A. J. Cosmol. Astropart. Phys., 2014, 08, 031.

Leinson, L.B., 2021. Impact of axions on the Cassiopeia A neutron star cooling. J. Cosmol. Astropart. Phys., 2021, 09, 001.

Leinson, L.B., 2022. Hybrid cooling of the Cassiopeia A neutron star. Mon. Not. R. Astron. Soc., 511, 5843.

Leinson, L.B., Pérez, A., 2006. Vector current conservation and neutrino emission from singlet-paired baryons in neutron stars. Phys. Lett. B, 638, 114.

Lifshitz, E.M., Pitaevskiĭ, L.P., Statistical Physics Pt. 2: Theory of the Condensed State, Pergamon Press, Oxford, 1980, §40.

Lim,Y., Holt, J.W., 2021. Proton pairing in neutron stars from chiral effective field theory. Phys. Rev. C, 103, 025807.

Margueron, J., Sagawa, H., Hagino, K., 2008. Effective pairing interactions with isospin density dependence. Phys. Rev. C, 77, 054309.

Negreiros, R., Schramm, S., Weber, F., 2013. Impact of rotation-driven particle repopulation on the thermal evolution of pulsars. Phys. Lett. B, 718, 1176.

Noda, T., Hashimoto, M., Yasutake, N., Maruyama, T., Tatsumi, T., Fujimoto, M., 2013. Cooling of compact stars with color superconducting phase in quark-hadron mixed phase. Astrophys. J., 765, 1

Page, D., 2016. NScool: Neutron star cooling code. Astrophys. Source Code Libr., record ascl:1609.009.

Page D., Prakash M., Lattimer J.M., Steiner A.W., 2011. Rapid cooling of the neutron star in Cassiopeia A triggered by neutron superfluidity in dense matter. Phys. Rev. Lett., 106, 081101.

Pavlov, G.G., Luna, G.J.M., 2009. A dedicated *Chandra* ACIS observation of the central compact object in the Cassiopeia A supernova remnant. Astrophys. J., 703, 910.

Pearson, J.M., Chamel, N., Potekhin, A.Y., Fantina, A.F., Ducoin, C., Dutta, A.K., Goriely, S., 2018. Unified equations of state for cold non-accreting neutron stars with Brussels–Montreal functionals – I. Role of symmetry energy. Mon. Not. R. Astron. Soc., 481, 2994; Erratum: 2019, Mon. Not. R. Astron. Soc., 486, 768.

Posselt, B., Pavlov, G.G., 2018. Upper limits on the rapid cooling of the central compact object in Cas A. Astrophys. J., 864, 135.

Posselt, B., Pavlov, G.G., 2022. The cooling of the central compact object in Cas A from 2006 to 2020. Astrophys. J., 932, 83.

Posselt, B., Pavlov, G.G., Suleimanov, V., Kargaltsev, O., 2013. New constraints on the cooling of the central compact object in Cas A. Astrophys. J., 779, 18.

Potekhin, A.Y., Chabrier, G., 2012. Thermonuclear fusion in dense stars. Electron screening, conductive cooling, and magnetic field effects. Astron. Astrophys., 538, A115.

Potekhin, A.Y., Chabrier, G., 2018. Magnetic neutron star cooling and microphysics. Astron. Astrophys., 609, A74.

Potekhin, A.Y., Chabrier, G., 2021. Crust structure and thermal evolution of neutron stars in soft X-ray transients. Astron. Astrophys., 645, A102.

Potekhin, A.Y., Fantina, A.F., Chamel, N., Pearson, J.M., Goriely, S., 2013. Analytical representations of unified equations of state for neutron-star matter. Astron. Astrophys., 560, 48.

Potekhin, A.Y., Pons, J., Page, D., 2015. Neutron stars – cooling and transport. Space Sci. Rev., 191, 239.

Potekhin A.Y., Chugunov A.I., Chabrier G. 2019, Thermal evolution and quiescent emission of transiently accreting neutron stars. Astron. Astrophys., 629, A88.

Potekhin, A.Y., Zyuzin, D.A., Yakovlev, D. G., Beznogov, M.V., Shibanov, Yu.A., 2020. Thermal luminosities of cooling neutron stars. Mon. Not. R. Astron. Soc., 496, 5052.

Reed, J.E., Hester, J.J., Fabian, A.C., Winkler, P.F., 1995. The three-dimensional structure of the Cassiopeia A supernova remnant. I. The spherical shell. Astrophys. J., 440, 706.

Sales, T., Lourenço, O., Dutra, M., Negreiros, R., 2020. Revisiting the thermal relaxation of neutron stars, Astron. Astrophys., 642, A42.

Schaab, C., Voskresensky, D., Sedrakian, A.D., Weber, F., Weigel, M.K., 1997. Impact of medium effects on the cooling of non-superfluid and superfluid neutron stars. Astron. Astrophys., 321, 591.

Schmitt, A., Shternin, P., 2018. Reaction rates and transport in neutron stars. In Rezzolla L., Pizzochero P., Jones D.I., Rea N., Vidaña I., eds, The Physics and Astrophysics of Neutron Stars. Springer, Heidelberg, p. 455.

Schwenk, A., Friman, B., Brown, G.E., 2003. Renormalization group approach to neutron matter: quasiparticle interactions, superfluid gaps and the equation of state. Nucl. Phys. A, 713, 191.

Sedrakian, A., Vertex renormalization of weak interactions in compact stars: Beyond leading order. 2012. Phys. Rev. C, 86, 025803.

Sedrakian, A., 2013. Rapid cooling of Cassiopeia A as a phase transition in dense QCD. Astron. Astrophys., 555, L10.

Sedrakian, A., 2016a. Axion cooling of neutron stars. Phys. Rev. D, 99, 065044.

Sedrakian, A., 2016b. Cooling compact stars and phase transitions in dense QCD. Eur. Phys. J. A, 52, 44.

Sedrakian, A., 2019. Axion cooling of neutron stars. II. Beyond hadronic axions. Phys. Rev. D, 93, 043011.

Sedrakian, A., Müthner, H., Schuck, P., 2007. Vertex renormalization of weak interactions and Cooper-pair breaking in cooling compact stars. Phys. Rev. C, 76, 055805.

Shternin, P.S., Yakovlev, D.G., 2015. Self-similarity relations for cooling superfluid neutron stars, Mon. Not. R. Astron. Soc., 446, 3621.

Shternin, P.S., Yakovlev, D.G., Heinke, C.O., Ho, W.C.G., Patnaude, D.J., 2011. Cooling neutron star in the Cassiopeia A supernova remnant: evidence for superfluidity in the core. Mon. Not. R. Astron. Soc., 412, L108.

Shternin, P.S., Baldo, M., Haensel, P., 2018. In-medium enhancement of the modified Urca neutrino reaction rates. Phys. Lett. B, 786, 28.

Shternin P.S., Ofengeim D.D., Ho W.C.G., Heinke C.O., Wijngaarden M.J.P., Patnaude D.J., 2021. Model-independent constraints on superfluidity from the cooling neutron star in Cassiopeia A. Mon. Not. R. Astron. Soc., 506, 709.

Shternin, P.S., Ofengeim, D.D., Heinke, C.O., Ho, W.C.G., 2023. Constraints on neutron star superfluidity from the cooling neutron star in Cassiopeia A using all *Chandra* ACIS-S observations. Mon. Not. R. Astron. Soc., 518, 2775

Steiner, A.W., Reddy, S., 2009. Superfluid response and the neutrino emissivity

of neutron matter. Phys. Rev. C, 79, 015802.
Takatsuka T., Tamagaki, R., 2004. Baryon superfluidity and neutrino emissivity of neutron stars. Prog. Theor. Phys., 112, 37.
Tamagaki, R., 1970. Superfluid state in neutron star matter. I. Generalized Bogoliubov transformation and existence of $^3P_2$ gap at high density. Prog. Theor. Phys., 44, 905.
Taranto, G., Burgio, G.F., Schulze H.J., 2016. Cassiopeia A and direct Urca cooling. Mon. Not. R. Astron. Soc., 456, 1451.
Thorne, K.S., 1977. The relativistic equations of stellar structure and evolution. Astrophys. J., 212, 825.
Tsiopelas, S., Sagun, V., 2020. Neutron star cooling within the equation of state with induced surface tension. Particles, 3, 693.
Tsiopelas, S., Sagun, V., 2021. Thermal evolution of neutron stars described within the equation of state with induced surface tension, Astron. Nachr., 342, 332.
Tu, Z., Li, A., 2025. Delayed thermal relaxation of rapidly cooling neutron stars: Nucleon superfluidity and non-nucleon particles. Astrophys. J., 987, 6.
Voskresensky, D.N., Senatorov, A.V., 1987. Description of nuclear interaction in Keldysh's diagram technique and neutrino luminosity of neutron stars. Sov. J. Nucl. Phys., 45, 411.
Wang, M., Audi, G., Wapstra, A.H., Kondev, F.G., MacCormick, M., Xu, X., Pfeiffer B., 2012. The AME2012 atomic mass evaluation. Chinese Phys. C, 36, 1603.
Wei, W., Xu, X.-Y., Wang, K.-T., Ma, X.-H., 2020. Roto-chemical heating with fall-back disk accretion in the neutron stars containing quark matter. Universe, 6, 62.
Wijngaarden, M.J.P., Ho, W.C.G., Chang, P., Heinke, C.O., Page, D., Beznogov, M., Patnaude, D.J., 2019. Diffusive nuclear burning in cooling simulations and application to new temperature data of the Cassiopeia A neutron star. Mon. Not. R. Astron. Soc., 484, 974.
Wiringa, R.B., Stoks, V.G.J., Schiavilla, R., 1995. Accurate nucleon-nucleon potential with charge-independence breaking. Phys. Rev. C, 51, 38.
Yakovlev, D.G., Levenfish, K.P., and Shibanov, Yu.A., 1999. Cooling of neutron stars and superfluidity in their cores. Phys. Usp., 42, 737.
Yakovlev, D. G., Kaminker, A. D., Gnedin, O. Y., Haensel, P., 2001. Neutrino emission from neutron stars. Phys. Rep., 354, 1.
Yang, S.H., Pi, C.-M., Zheng, X.-P., 2011. Rapid cooling of the neutron star in Cassiopeia A and r-mode damping in the core. Astrophys. J., 735, L29.